 doi:10.20944/preprints202007.0274.v1

# Title:

Growth and characterization of polycrystalline n-silicon thin films for photocatalytic splitting of water in oxide-silicon tandem cells


## Authors:

Ali Zahid [a†], Umer Zahid [b], Aamir Hasan [c], Muhammad Khuldoon [d]

## Affiliations:

[a †] Jülich Centre for Neutron Science, Forschungszentrum Jülich GmbH, Jülich, Germany
[b] Department of Mechanical and Aerospace Engineering, Politecnico di Torino, Turin, Italy
[c] Dhanani School of Science and Engineering, Habib University, Karachi, Pakistan
[d] Mechanical Engineering Division, Pakistan Navy, Karachi, Pakistan

## ORCID:

[†]Ali Zahid | 0000-0001-5211-5289
Umer Zahid | 0000-0002-8623-8313
Muhammad Khuldoon | 0000-0002-9772-5037

## [†] Corresponding author:

Ali Zahid | Email: ali.zahid@outlook.de; Tel. (+92) 3323106687


## Abstract:


With the decline in fossil fuels, hydrogen-based alternatives provide a reliable and clean source for sustainable energy generation. In these endeavors, photochemical splitting for hydrogen production through tandem cells has been the source of much theoretical and experimental research in science. Much focus has been placed on interfacial band gap engineering as one of the most promising routes in the generation of hydrogen. This present work explores sputtering of n-silicon to form the active electrode in a n-Si | n-$TiO_2$ tandem cell and investigates the effect of variations in sputtering and post sputtering treatment parameters (rapid thermal annealing and long cycle annealing) for successful deposition of crystalline Silicon. The samples were successfully characterized via Raman Spectroscopy, X-ray Diffraction and Optical Transmission Spectroscopy to ascertain prevalent crystalline order and optical band gap, under different sputtering and post-sputtering conditions. Relevant conclusions to ascertain the best possible n-Si deposition parameters indicated the use of post-sputtering annealing to induce and enhance crystallinity but to be cautious as not to incur the loss of Si during the annealing process.


**Keywords:** tandem cells, magnetron sputtering, Raman Spectroscopy, X-Ray Diffraction, silicon deposition, Optical Transmission Spectroscopy, photocatalytic conversion, hydrogen production, post-sputtering treatments

 doi:10.20944/preprints202007.0274.v1

# 1. Introduction

In the last decade, there has been considerable research endeavours in photocatalytic conversion of water (splitting water into $O_2$ and $H_2$) for hydrogen evolution resulting in numerous process optimizations. Recently, tandem solar cells or multi-junction solar cells have been quite successful in evolving large volumes of hydrogen [1-9, 11]. A tandem solar cell is composed of two or more solar cells of different materials stacked together. Each of the solar cells is optimized to a specific wavelength range. Hence, together these stacks of solar cells can absorb a wider range of wavelengths leading to higher quantum efficiency.

This arrangement of different solar cells, made of different materials with individual characteristic properties, offer the possibility of fine-tuning individual band gaps. Normally, a small portion of the solar spectrum is absorbed by a specific band gap, characteristic of the material, producing a relatively smaller photochemical conversion. But in a tandem solar cell, by using different materials, each with their own distinctive band gaps, a single photosystem can be designed, possessing an optimal band gap for absorbing a large portion of the solar spectrum [2 - 7].

For tandem solar cells, both indirect semiconductors, as well as combinations of direct III-V semiconductors are used. The aim is to absorb light of the correct wavelength(s) attuned to the specific solar cell layer. A tandem cell for photo-chemical splitting of water consists of two photosystems connected in series. The initial photosystem is a solar cell comprising of a counter electrode and a working electrode which can be created from a semiconductor thin film [4, 10]. This system produces a positive potential which can be used to oxidize water, but the energy output is insufficient for direct hydrogen production. Longer wavelengths of the light are passed onwards to a secondary photosystem, like, a dye sensitized titanium dioxide solar cell, producing electric potential under all possible wavelengths in the spectrum. These two photosystems form 2 separate electrodes and in combination generate enough potential for water splitting [6, 7, 10].

By depositing different layers of thin films, it is possible to construct a tandem cell with desirable properties, particularly, acquiring a tailored band gap for optical absorption [1-5]. Different layers of the tandem cell contribute to either the cathodic or anodic potential by production of electron-hole pairs. These stacks of different layers have variable thickness depending on the required properties of the tandem cell and are largely interface dependent i.e. their optical properties are dictated by their interface. The optical properties of such a tandem cell is characterized by the wavelengths absorbed by all the layers [4]. The smaller wavelengths absorbed by the initial photosystem induces excitation of the valence band in the thin film semiconductor resulting in the creation of an electron-hole pair. Hole migration into the electrode/electrolyte interface occurs subsequently and water is oxidized into oxygen. The electrons produced during the reaction in the first photosystem do not have energy to reduce hydrogen and are transferred into the secondary photosystem by injecting them in the conduction band of n-titanium dioxide. The overall electrons produced, in the secondary photosystem, reduce hydrogen at the cathode [4, 8].

Detailed mechanisms for the evolution of hydrogen from water is complex and involves intermediate elementary reaction steps. It is also acknowledged that the majority of over-potentials and losses in any water splitting system are accompanied with the oxygen evolution reaction. Recent studies have shown that metal oxides such as $WO_3$, $Nb_2O_5$, $V_2O_5$, $Ta_2O_5$, $TiO_2$, Ir $(OH)_3$ and $CeO_2$ absorb light effectively and possess good electro-photonic properties. These materials are hence suitable for use at photo-electrodes for splitting of water in tandem-cells [4, 5, 7, 10, 11], but are complicated to synthesis due to their transition element nature. Thus, research endeavours should also be directed towards making use of already prevalent materials that are easier to synthesize and have controllable physical properties.

This present work investigates the deposition of n-Silicon (n-Si) thin films using dc magnetron sputtering and their characterization to ascertain optimal conditions, for deposition and achieving high level of crystallinity for applicability in photocatalytic tandem cells.

Preprints (www.preprints.org) | NOT PEER-REVIEWED | Posted: 13 July 2020 doi:10.20944/preprints202007.0274.v1

# 2. Theoretical Background

## 2.1. Photochemical Splitting of Water

The splitting of water into its components, hydrogen, and oxygen, can be accomplished by utilizing solar energy through a photo-electro-chemical process. In a photo-electro-chemical system, water splitting occurs at the cathode and anode where excited electrons in the conduction band and holes in the valance band participate, respectively.

The process can be represented as follows:

**Photo-electrochemical splitting of water**

$$4h\nu + 2H_2O_{(aq)} \longrightarrow O_{2(g)} + H_{2(g)}$$

The photocatalytic conversion process efficiency is tainted by energy losses due to over-potentials leading to an increase from the 1.23 V actually required voltage for the splitting of water [1], equivalent to energy with a wavelength of approximately 1000 nm [3, 4, 5]. Hence, if energy is efficiently utilized, water splitting can be achieved by radiation in the visible range of the electromagnetic spectrum [7]. Water itself is not capable of absorbing radiation in the visible spectrum hence it is imperative for direct conversion systems to find a light-harvesting mechanism and a catalyst that can competently collect solar energy, transmute it into chemical energy in form of electron/hole pairs and direct it towards the water splitting reaction [5].

Semiconductor electrodes, like Silicon (Si), can absorb photons with energy greater than the characteristic band gap energy under illumination and produce significant electron/hole pairs, Figure 1. Both excited electrons in the conduction band and holes in the valence band participate in the water splitting process. For an n-type semiconductor, the semiconductor electrode will act as a photo-anode. When an n-type semiconductor electrode is subjected to a band-gap illumination, water is oxidized by photo generated holes in the valence band. Simultaneously, electrons in the conduction band at the counter-electrode reduce water into hydrogen. If the band edges of the semiconductor are not thermodynamically appropriate for direct water splitting, a bias potential must be applied [6].

The hydrogen evolution reaction on the counter electrode is kinetically faster and requires a comparatively lower over-potential ($\eta_{H2}$). However, the reaction for the evolution for oxygen is kinetically slower and requires a higher over-potential ($\eta_{O2}$), Figure 2. To compensate for the additional energy required for over-potential losses, photons with energy equal and more than 1.23 V are required [13]. Continuous water splitting requires the current due to hydrogen reduction to be equal to the current for oxygen generation ($I_{H2} = I_{O2}$). It is also worth mentioning that water splitting can be achieved without the application of an electric current, if the following 3 conditions are met [1, 3, 7]:

a. Oxygen evolution occurs at a potential comparatively more negative at which hydrogen evolution occurs.
b. Hydrogen evolution occurs at a potential comparatively more positive at which oxygen evolution occurs.
c. Potential for hydrogen evolution is made more positive and that for oxygen evolution is made more negative, until the former is more positive than the latter.

Preprints (www.preprints.org) | NOT PEER-REVIEWED | Posted: 13 July 2020 doi:10.20944/preprints202007.0274.v1

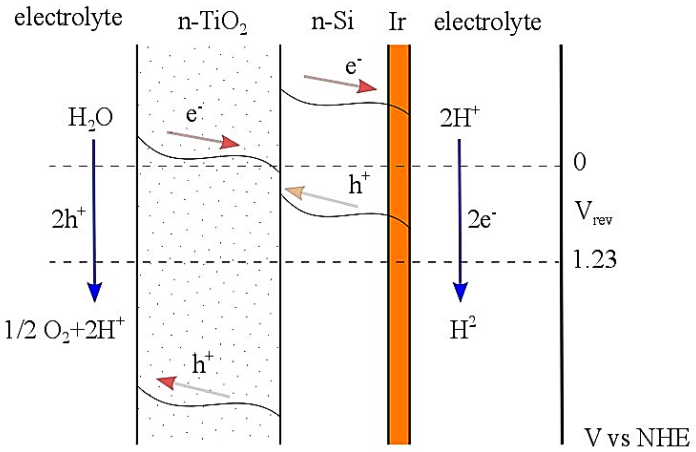


Figure 1: Production of electron-hole pairs and the electrochemical process for water splitting exemplified by a tandem cell configuration for hydrogen generation via n-$TiO_2$/n-Si/Ir. [12]

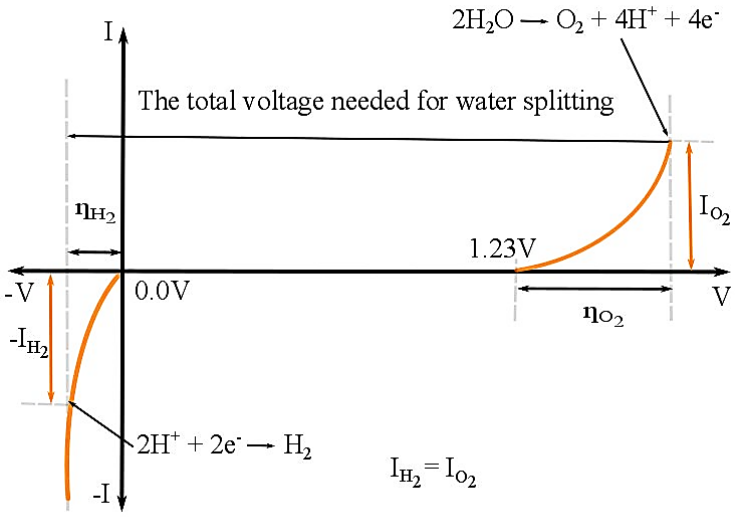


Figure 2: Electrode potentials for photochemical splitting of water. Hydrogen and oxygen evolution, at cathode and anode respectively, is shown [13].

Preprints (www.preprints.org) | NOT PEER-REVIEWED | Posted: 13 July 2020 doi:10.20944/preprints202007.0274.v1

## 2.2. Semiconductor materials for direct water splitting

Any semiconductor used for the purpose of photo-chemical water splitting must fulfil certain criteria. These criteria are briefly enumerated below and are by no means exhaustive.

**- Band gap energy**

An optimum candidate should not have a band gap much larger than the required energy for photocatalytic conversion of water [7]. The optimum band gap for most photovoltaics is between 1.20 eV and 1.40 eV [8, 10]. The energy difference between the redox reactions between hydrogen and oxygen evolution is 1.23 eV. Suitable candidates for photo-electrodes should have a band gap greater than 1.23 eV to compensate for over-potential associated with oxygen evolution and recombination [7, 13].

**- Positioning of the band gap**

For oxygen evolution [10]: The quasi-Fermi energy of the holes must be below that of oxygen evolution, $\mathcal{E}_F$ ($H_2O$ | $O_2$), indicating that the valence band edge $\mathcal{E}_v$ should be below oxygen evolution.

For hydrogen evolution [10]: The quasi-Fermi energy of the electrons must be energetically above the hydrogen evolution, $\mathcal{E}_F$ ($H^+$ | $H_2$), indicating that the conduction band edge $\mathcal{E}_c$ should be above hydrogen evolution.

If these criteria are not satisfied an additional potential bias must be applied, which diminishes the overall conversion efficiency of the system.

**- Charge separation and interfacial kinetics**

Immediate charge separation is mandatory for a semiconductor photovoltaic once the electrons from the valence band are excited to the conduction band [15]. This implies that charge and hole mobility are optimal in the material. This can be achieved by having a low density of band gap states. These band gap states are a consequence of impurities, irregular crystal structures, grain boundaries and interactions with other medium. Fast interfacial kinetics of the system is also crucial for water splitting application and can be improved by using an oxygen catalyst like $RuO_2$ [17].

**- Stability**

With decreasing band gap, the stability of semiconductors decreases in a redox system thus putting a limitation on the number of candidates suitable for photo-chemical water splitting [14]. Illumination itself causes damage to the semiconductor material as the photo-induced holes are reactive and can cause oxidation of the material. Most of the III-IV semiconductors, Figure 3, show promise for water splitting due to their combined small band gap that can be attuned to a large fraction of the solar spectrum and suitable band edge positions [14]. But their large tendency for dissolution and photo-corrosion inhibits their use as photo-electrodes in direct water contact [12].

Preprints (www.preprints.org) | NOT PEER-REVIEWED | Posted: 13 July 2020 doi:10.20944/preprints202007.0274.v1

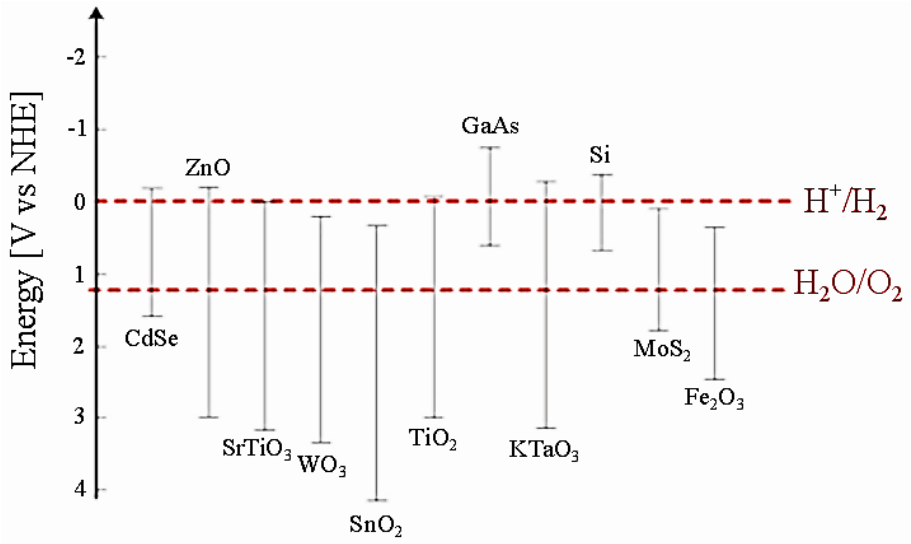


Figure 3: Band gaps of commonly used semiconductors for photovoltaic applications [14].

## 2.3. Low-temperature approach for the synthesis of crystalline Silicon thin films

Deposition of Si thin films at lower temperatures has the added benefit of choosing from a variety of substrate materials. Since the growth is limited to temperatures ~ 600$^o$C, materials like float glass, steel, plastic films, high temperature borosilicate glass and soda lime glass can be used as substrates. As diffusion is comparatively hindered at lower temperatures, contamination problems are usually reduced.

One of the main advantages of using a low temperature approach is that there is a significant reduction in the stress of the deposited Si film due to thermal expansion and the active layer from the substrate can be reduced. [17]. Successful commercialization requires that a suitable inexpensive substrate, high deposition rate and easy to follow methodology be forthcoming. For high carrier collection probability, the effect diffusion length must be greater than the width of a cell which can be possible by having the grain size greater than the cell width or by having electrically inactive grain boundaries.

The low temperature approach has a drawback of producing smaller grain sizes and deposition rates than required for optimal efficiency. The low temperature approach for c-Si deposition has a growth rate limited at between 3 nm min$^{-1}$and 10 nm min$^{-1}$ and thus is the limiting factor for industrialization of this process. Different grain sizes are achievable depending on the deposition conditions. In a study by E. Vallat-Sauvain [18] Si deposited by rf-sputtering at substrate temperatures below 400$^o$C resulted in nano or micro-crystalline grains whereas at a substrate temperature above 600$^o$C polycrystalline grains were obtained.

A higher density of larger grains usually results in higher efficiency and hence more often the film is recrystallized to engineer the desirable grain size and structure. Low temperature recrystallization methods such as rapid thermal annealing (RTA), solid phase laser and e-beam and metal induced recrystallization are widely employed [18]. Using glass as the substrate material has the disadvantage of lacking suitable surface passivation at the glass-Si interface. Further a glass substrate can also result in the possibility of impurities diffusing from the substrate into the deposited Si film and the thermal expansion coefficient of both the glass and deposited Si has a large mismatch [19].

Engineering the grain size is a very significant consideration for low temperature depositions and dominates electrical transport properties for Si thin films [20]. Depositions at lower temperatures lead to the formation of micro and crystalline Si grains whereas depositions at higher temperatures results in the

Preprints (www.preprints.org) | NOT PEER-REVIEWED | Posted: 13 July 2020 doi:10.20944/preprints202007.0274.v1

evolution of polycrystalline grains [21, 22, 23]. Considering the relevance of grain size towards solar cell applications, it has been argued that nano or micro-crystalline Si grains culminates in a material which lifecycle is largely influenced by trapping or recombination and thus necessitates a p-i-n cell structure whose intrinsic regions are utilized to distinguish regions of high recombination from regions where charge separation takes place. Poly-Si grains are usually required for the formation of a p-n junction cell which allows high voltage values when compared to p-i-n cells [24]. These cells are widely sought after if the potential barriers at the grain boundaries do not influence recombination effects in the solar cell.

The initial publishing regarding µ-Si is attributed to a cooperation between Fuji Electric Corporation and Kawasaki Heavy Industries [20]. They reported deposition of µ-Si:H by electron beam excited plasma (EBEP) chemical vapor deposition (CVD) on Corning 7059 glass substrates at temperature of 240°C. An increase in deposition rate was observed at higher $SiH_4$ flow rate but was the process resulted in a decreased crystallinity and grain size. There was no strong correlation between the deposition rate and substrate temperature. The film structure and grain formation were, concludingly, dependent on reactions with the plasma. The plasma formed in the EBEP CVD process was under 3.5 Pa and its characteristics were largely dependent on the $SiH_4$ flow. Interestingly, µ-Si thin films with a 100% crystalline fraction were created at South Bank University by also using a Corning 7059 glass substrate. The µ-Si film was deposited using electron resonance Plasma Assisted CVD (ECR PACVD) technique at a substrate temperature of 500°C [25].

## 2.4. Recrystallization and annealing of deposited Si thin films

After the deposition of Si on a suitable substrate, several enhancements to the microstructural properties of the thin film is, at certain times, necessary and beneficial. This improvement can be tailored through recrystallization of the already deposited crystalline film. Recrystallization can also increase the crystallization percentage of the grains present in the material which is very effective to augment optical and electrical transport phenomenon.

High temperature recrystallization techniques are mostly focused on zone melting recrystallization (ZMR) and is not relevant to this work. Low temperature recrystallization techniques include laser recrystallization (LR), solid phase recrystallization (SPR), rapid thermal process (RTP) and vacuum furnace annealing. Solid Phase Re-crystallization (SPR) is advantageous in terms of low cost, low operating temperature and results in the production of a high-quality active layer. SPR is normally carried out at temperatures below 500°C for microcrystalline Si and temperatures above 500°C have shown to cause grain coarsening [26]. RTP or rapid thermal annealing (RTA) allows the nucleation process to occur at temperatures near the melting point of Si without melting the Silica glass substrate. It is well demonstrated that the nucleation rate is low near the melting point of Si; hence grain sizes obtained with RTA are generally larger [27, 28].

Of particular importance is the work done by Lambertz et.al [29] in which grain sizes up to 1 micron were realized on Corning 1737 alumino-silicate glass using DC magnetron sputtering. The resulting structure was initially amorphous in nature and was then subsequently recrystallized with SPC to from micro crystalline Si. The sputtering process was done in a vacuum of 0.5 Pa using deposition temperatures from 25°C to 600°C. At 25°C significant peeling prior SPC was observed and at 600°C a highly crystalline region was reported prior to the SPC process. No amorphous regions were detected but large defects were present. No difference in grain size was seen after SPC for the deposition temperatures between 200°C and 400°C. This methodology and results are analogous to what has been achieved in this present work.

Recrystallization and annealing mediated by lasers have also been quite successful in the production of µm Si grains. They have the added advantage of localizing the energy density on the sample and cause less heat propagation. In a work by R.L. Wallace et.al. [30] pulsed laser technique was employed to induce crystallization in amorphous Si:H film. The Si:H film was deposited on a molybdenum (Mo) substrate by

Preprints (www.preprints.org) | NOT PEER-REVIEWED | Posted: 13 July 2020 doi:10.20944/preprints202007.0274.v1

using a DC glow discharge at 300°C. Annealing was carried out with a Nd: glass pulsed laser resulting in grain sizes more than 0.2 µm and a minority carrier diffusion length of 22 µm. The hydrogen passivation of grain boundaries was responsible for the high diffusion length.

In a very recent work by Louise R. Bailey et.al. [31] pulsed DC magnetron sputtering was used to deposit hydrogen free Si films on a glass substrate. Characterization of these films was carried out using micro-Raman spectroscopy and showed a large crystalline fraction for annealing in a vacuum tube at 1000°C for 2 hours. The micro-Raman spectra showed in Figure 4 depicts a very sharp peak for Si at these parameters. The work done by Louise R. Bailey et.al. [31] is somewhat comparable to our work. Si thin films of up to 20-30 µm were deposited using this methodology with a deposition rate of over 20 nm $min^{-1}$.

Pulsed rapid thermal annealing of Si has also had its share of research activities largely focusing on a prior low temperature route for thin film deposition, like sputtering, and subsequent PRTA to induce crystallinity. This post-sputtering methodology is encountered in a work done by Koji Yamasaki et.al. [32] in which initial low temperature deposition of amorphous Si was done using metal nanoparticle synthesized with a protein cage. The subsequent annealing step is of prime importance with respect to this present work. PRTA was carried out for a variation of temperature from 10s to 60s over a range of temperatures from 300°C to 550°C as shown in Figure 5a. An average crystallite grain diameter of 5 µm was reportedly achieved in 60s, with temperatures up to 740°C (Figure 5b). Another work by R.Gunawan et.al. [33] exhibited the PRTA process by modelling the relevant parameters necessary for controlling the process. Their process modelling indicated that during the PRTA process the heating and cooling stages are the notable constraints. Temperatures more than 1111°C are relevant for the much-needed activation of the annealing process and give rise to necessary diffusion steps, for nuclei formation and growth, by overcoming the diffusion barrier.

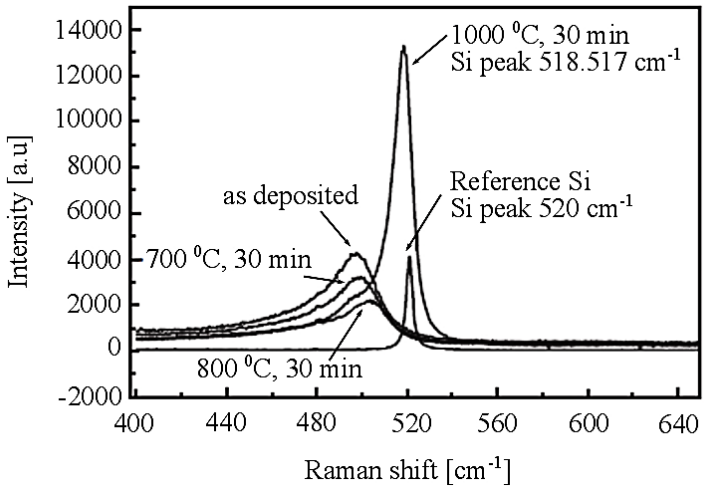


Figure 4: Raman spectrum of Si processed at different temperatures. A higher annealing time produces a sharper Raman active Si peak [31].

Preprints (www.preprints.org) | NOT PEER-REVIEWED | Posted: 13 July 2020 doi:10.20944/preprints202007.0274.v1

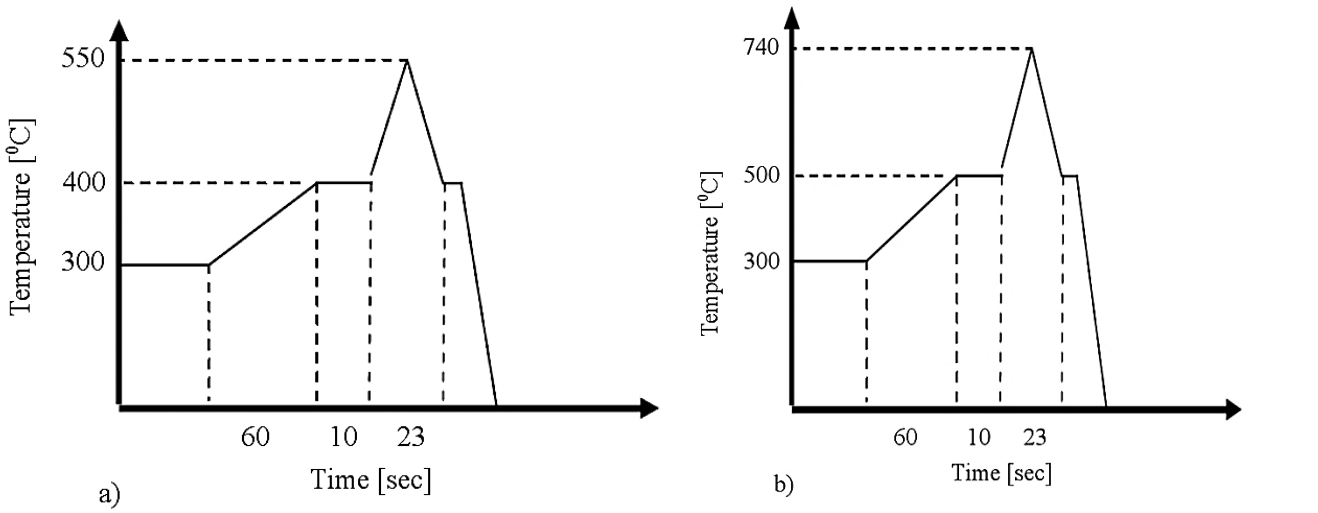


Figure 5 (a, b): Typical Rapid Thermal Annealing (RTA) profiles for post sputtering treatment of Si [32].

Preprints (www.preprints.org) | NOT PEER-REVIEWED | Posted: 13 July 2020 doi:10.20944/preprints202007.0274.v1

# 3. Experimental Procedure

In this work deposition of Si thin films was achieved on amorphous Silica wafers under ambient and high temperatures. The deposited Si thin films were subjected to 2 different annealing cycles, rapid thermal annealing (RTA) and long cycle annealing (AN), under the influence of different working gas mixtures, namely, hydrogen and a combination of argon and hydrogen. The deposited Si thin films were characterized using Raman Spectroscopy, X-ray diffraction, and Optical Ellipsometry to assess the nature of bond formation in the deposited samples and theoretical calculations of the optical band gap. 10 samples, each, were prepared for all the protocols enumerated in Table 1, 2, and 3.

## 3.1. Sputtering

The deposition of Si thin films was carried out on an amorphous silica wafer substrate with the dimensions 100 mm x 500 mm. The silica wafer substrate was reduced to 1cm x 1cm using a very thin diamond coating steel wire. Prior to the sputtering process, the substrates were cleaned ultrasonically in propanol and acetone, separately, to avoid the accumulation of oil and dirt residue on the surface. The samples were also subjected to a pre-sputtering treatment for 200s before the start of the actual sputtering experiment.

Table 1 depicts the sputtering experimental protocols employed for the deposition process. The experiments were designed such that comparisons can be made for the use of different working gases, deposition temperatures, dc power imparted to the plasma and sputtering time. The target material for the experiment was n-doped Si with phosphorous, having a conductivity of 0.015 - 0.06 Ω cm.

For the experiments done at 200 ºC, the substrate was heated up to 200 ºC at a heating rate of 25 ºC $min^{-1}$ prior to the sputtering process, the substrate was sputtered subjected to relevant protocols (Table 1) and the temperature was maintained till the conclusion of the sputtering process. The samples were then allowed to cool down to room temperature (27 ºC) and placed in the sample box to minimize atmospheric contact.

| **Protocol** | **Gas** | **Gas pressure** [mbars] | **Gas flow rate** [sccm] | **Power** [watt] | **Temperature** [˚C] | **Time** [sec] | **Thickness** [nm] |
|---|---|---|---|---|---|---|---|
| 1 | Ar | 0.02 | 30 | 300 | RT | 600 | 240 - 260 |
| 2 | Ar | 0.02 | 30 | 300 | RT | 1200 | 380 - 400 |
| 3 | Ar | 0.02 | 30 | 400 | RT | 1200 | 600 - 650 |
| 4 | Ar | 0.02 | 30 | 400 | 200 | 1800 | 1000 - 1050 |
| 5 | Ar | 0.02 | 30 | 400 | RT | 1800 | 1000 - 1050 |
| 6 | Ar | 0.02 | 30 | 400 | 200 | 2400 | 1250 - 1300 |
| 7 | Ar + $H_2$ (6%) | 0.02 | 30 | 300 | RT | 1200 | 360 - 400 |
| 8 | Ar + $H_2$ (6%) | 0.02 | 30 | 400 | RT | 1200 | 600 - 650 |
| 9 | Ar + $H_2$ (6%) | 0.02 | 30 | 400 | 200 | 2400 | 1250 - 1300 |

Table 1: Protocols for the sputtering process (Ar: Argon gas; $H_2$: Hydrogen Gas).

The substrates were pre-cleaned in the sputtering environment for 200s to cleanse the substrate prior to deposition, by using highly energetic particles already formed in the plasma. Careful monitoring of the substrate was undertaken during the pre-sputtering process to prevent any additional roughening of the surface and possible overheating.

To decide the amount of dc-power applied to the plasma, multiple experiments from 100W to 400W were carried out while assessing the thickness of the thin film deposited using Veeco Dektak $6M^R$ Profilometer,

Preprints (www.preprints.org) | NOT PEER-REVIEWED | Posted: 13 July 2020 doi:10.20944/preprints202007.0274.v1

Figure 6 shows the variation of the deposited film thickness with the power. A decision was made to keep the film thickness above 250 nm so as to allow for sufficient deposited material for stress relaxation during annealing, to avoid evaporation of the deposited Si at high temperatures during the rapid thermal annealing and long cycle annealing steps. Characterization of films with thickness above 250 nm is also easier as there is a clear distinction between the film, interface, and substrate.

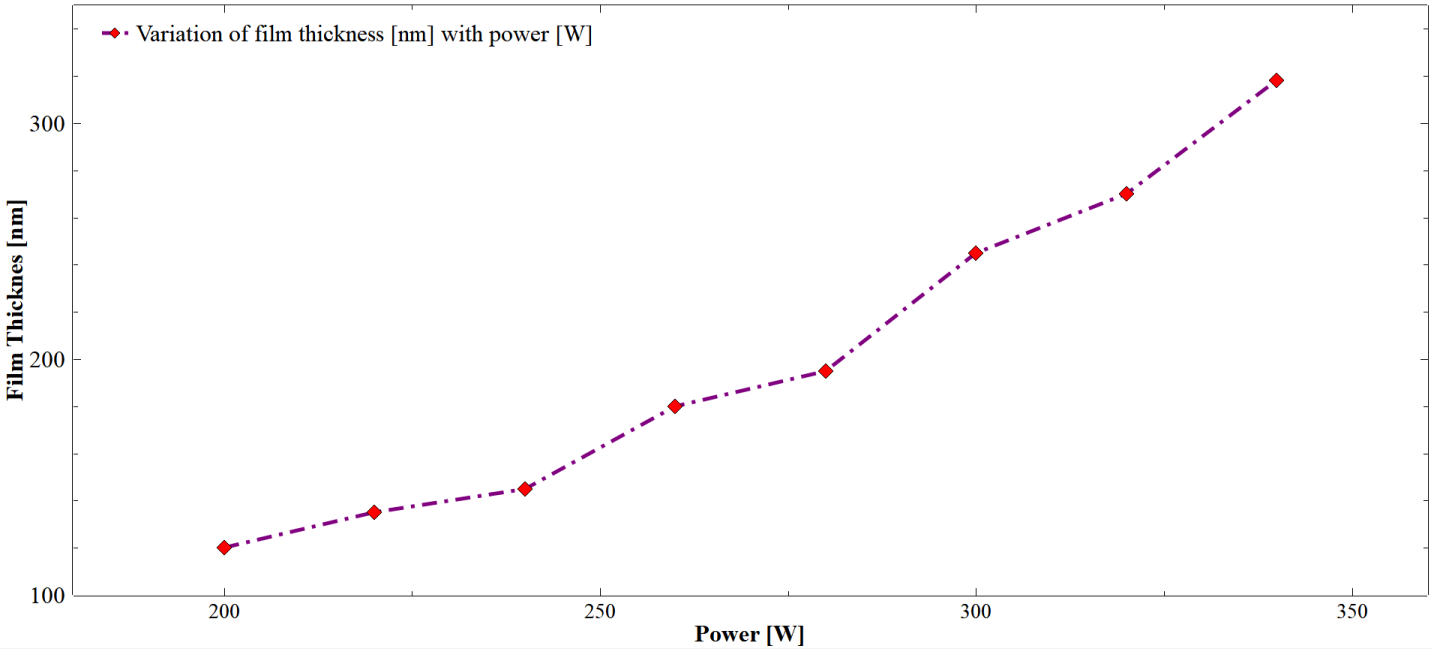


Figure 6: Variation in deposited film thickness (nm) with sputtering power at different power input(s) to the plasma, for 600 s, at room temperature

Preprints (www.preprints.org) | NOT PEER-REVIEWED | Posted: 13 July 2020 doi:10.20944/preprints202007.0274.v1

## 3.2. Rapid Thermal Annealing

After the sputtering process, some of the samples were introduced to rapid thermal annealing. The temperature of the selected substrates was sharply increased to the desired value under Ar and Ar + $H_2$(6%) atmosphere, Table 2. The process was carried out in an enclosed sealed chamber, using the desired working gas, and applied to a rapid thermal annealing cycle optimized from the work done by Koji Yamasaki et.al. [32], Figure 5.

| No. | Working gas | Temperature [°C] | Time [sec] |
|---|---|---|---|
| 1 | Ar & Ar + $H_2$ (6%) | 750 | 15 |
| 2 | Ar & Ar + $H_2$ (6%) | 1040 | 200 |
| 3 | Ar & Ar + $H_2$ (6%) | 800 | 60 |
| 4 | Ar & Ar + $H_2$ (6%) | 1040 | 600 |

Table 2: Protocols for the rapid thermal annealing process

(Ar: Argon gas; $H_2$: Hydrogen Gas).

## 3.3. Long Cycle Annealing

To increase the crystallinity of the samples long cycle annealing was also carried out sputtered samples. Table 3 shows the parameters for the annealing experiments. Some samples were subjected to long cycle annealing after the rapid thermal annealing process to ascertain, whether a secondary post sputtering processing step can enhance crystallinity. The annealing step was optimized from a relevant work done by Koji Yamasaki [32] which concluded the optimal annealing cycle above 800 ºC and below 1200 ºC.

| No. | Working gas | Temperature [°C] | Time [sec] |
|---|---|---|---|
| 1 | Ar | 800 | 36000 |
| 2 | Ar | 1000 | 3600 |
| 3 | Ar & Ar + $H_2$(6%) | 1050 | 3600 |
| 4 | Ar & Ar + $H_2$(6%) | 1000 | 3600 |

Table 3: Protocols for the long cycle annealing process.

(Ar: Argon gas; $H_2$: Hydrogen Gas).

Preprints (www.preprints.org) | NOT PEER-REVIEWED | Posted: 13 July 2020 doi:10.20944/preprints202007.0274.v1

# 4. Characterization

## 4.1. Raman Spectroscopy

Raman spectroscopy was carried out on the deposited samples using a Horiba T64000 Triple Raman Spectrometer$^{R}$ system. The source consisted of an Ar laser with a wavelength of 514.53 nm coupled with a plasma line-filter outside the source. The desired wavelength of light was incident towards the microscope using a complex array of optical arrangements, where it irradiated the sample placed on a stage underneath the microscope. The microscope, comprising of an objective lens, served the dual purpose of focusing the incident light on the sample and to collect the scattered light from the sample. Since the scattered light consists of both Rayleigh and Raman scattering, an edge filter is used to selectively diminish the Rayleigh scattering. The remaining Raman scattering was subjected to a line diffracting spectrometer and the resultant spectrum is projected onto a CCD camera to optimally configure the signal to noise ratio. The corrected spectra were then observed on a monitor screen.

The samples for the Raman Spectroscopy were chosen such to compare the deposition parameters, the post sputtering processes and investigate their influence on the formation of the Si atomic order. The representative samples from Tables 1, 2, and 3, subjected to Raman Spectroscopy and their processing history are depicted in Table 4. The sample groups in Table 4 are representative of 10 samples, each, subjected to a particular sputtering and/or annealing cycle.

| Sample | Sputtering | | | | Rapid Thermal Annealing | | | Long Cycle Annealing | | |
|---|---|---|---|---|---|---|---|---|---|---|
| Group No. | Working gas | Power [watt] | Temperature [°C] | Time [sec] | Gas Used | Temperature [°C] | Time [sec] | Gas Used | Temperature [°C] | Time [sec] |
| R-1 | Ar | 300 | RT | 600 | - | - | - | - | - | - |
| | Ar | 300 | RT | 1200 | - | - | - | - | - | - |
| R-2 | Ar + $H_2$ (6%) | 300 | RT | 1200 | - | - | - | - | - | - |
| | Ar + $H_2$ (6%) | 300 | RT | 1200 | Ar + $H_2$ (6%) | 1000 | 200 | - | - | - |
| | Ar + $H_2$ (6%) | 300 | RT | 1200 | - | - | - | Ar + $H_2$ (6%) | 1000 | 3600 |
| R-3 | Ar | 400 | RT | 1200 | - | - | - | - | - | - |
| | Ar | 400 | RT | 1200 | Ar | 1000 | 200 | - | - | - |
| | Ar | 400 | RT | 1200 | - | - | - | Ar | 1000 | 3600 |
| R-4 | Ar + $H_2$ (6%) | 400 | RT | 1200 | - | - | - | - | - | - |
| | Ar + $H_2$ (6%) | 400 | RT | 1200 | Ar + $H_2$ (6%) | 1000 | 200 | - | - | - |
| | Ar + $H_2$ (6%) | 400 | RT | 1200 | - | - | - | Ar + $H_2$ (6%) | 1000 | 3600 |
| R-5 | Ar | 400 | RT | 1800 | - | - | - | - | - | - |
| | Ar | 400 | RT | 1800 | | | | Ar + $H_2$ (6%) | 1050 | 3600 |
| | Ar | 400 | RT | 1800 | | | | Ar | 1050 | 3600 |
| | Ar | 400 | RT | 1800 | Ar | 1000 | 200 | | | |
| R-6 | Ar | 400 | RT | 1800 | - | - | - | - | - | - |
| | Ar | 400 | 200 | 1800 | Ar | 1000 | 200 | - | - | - |
| | Ar | 400 | 200 | 1800 | - | - | - | Ar | 1000 | 3600 |
| R-7 | Ar + $H_2$ (6%) | 400 | 200 | 1800 | - | - | - | - | - | - |
| | Ar + $H_2$ (6%) | 400 | 200 | 1800 | Ar + $H_2$ (6%) | 1000 | 200 | - | - | - |
| | Ar + $H_2$ (6%) | 400 | 200 | 1800 | - | - | - | Ar + $H_2$ (6%) | 1000 | 3600 |
| R-8 | Ar | 400 | 200 | 2400 | - | - | - | - | - | - |
| | Ar | 400 | 200 | 2400 | Ar | 1000 | 200 | - | - | - |
| | Ar | 400 | 200 | 2400 | - | - | - | Ar | 1000 | 3600 |
| R-9 | Ar | 400 | 200 | 2400 | - | - | - | - | - | - |
| | Ar + $H_2$ (6%) | 400 | 200 | 2400 | Ar + $H_2$ (6%) | 1000 | 200 | - | - | - |
| | Ar + $H_2$ (6%) | 400 | 200 | 2400 | - | - | - | Ar + $H_2$ (6%) | 1000 | 3600 |

Table 4: Processing history of the samples subjected to Raman Si Spectroscopy. For each sample group, 10 samples were prepared for investigations.

(Ar: Argon gas; $H_2$: Hydrogen Gas).

Preprints (www.preprints.org) | NOT PEER-REVIEWED | Posted: 13 July 2020 doi:10.20944/preprints202007.0274.v1

To investigate the formation of possible Si-H compounds and hydrogen inclusions, in the deposited Si thin films, localized probing through Raman Spectroscopy in the 600 $cm^{-1}$ to 2500 $cm^{-1}$ range was also carried out. During the sputtering and annealing experiments inquiries were made to ascertain the crystallinity of the deposited Si thin films by using Ar + $H_2$ (6%) gas during the process.

Si forms Si-H, Si-$H_2$ and Si-$H_3$ in the presence of $H_2$ at high temperatures, each with their own distinctive Raman frequencies [34]. Table 5 shows the processing history of the samples subjected to Raman Si:H analysis. The sample groups in Table 5 are representative of 10 samples, each, subjected to a particular sputtering and/or annealing cycle.

| Sample | Sputtering | | | | Rapid Thermal Annealing | | | Annealing | | |
|---|---|---|---|---|---|---|---|---|---|---|
| Group No. | Working gas | Power [watt] | Temperature [˚C] | Time [sec] | Gas Used | Temperature [˚C] | Time [sec] | Gas Used | Temperature [˚C] | Time [sec] |
| RSH-1 | Ar + $H_2$ (6%) | 300 | RT | 1200 | - | - | - | - | - | - |
| | Ar + $H_2$ (6%) | 300 | RT | 1200 | Ar + $H_2$ (6%) | 800 | 60 | - | - | - |
| | Ar + $H_2$ (6%) | 300 | RT | 1200 | - | - | - | Ar | 800 | 3600 |
| RSH-2 | Ar + $H_2$ (6%) | 400 | 200 | 1800 | - | - | - | Ar + $H_2$ (6%) | 1000 | 3600 |
| | Ar + $H_2$ (6%) | 400 | 200 | 1800 | Ar + $H_2$ (6%) | 800 | 60 | - | - | - |
| | Ar + $H_2$ (6%) | 400 | 200 | 1800 | - | - | - | Ar + $H_2$ (6%) | 1000 | 3600 |

Table 5: Processing history of the samples subjected to Raman Si:H Spectroscopy. For each sample group 10 samples were prepared for investigations.

(Ar: Argon gas; $H_2$: Hydrogen Gas).

Preprints (www.preprints.org) | NOT PEER-REVIEWED | Posted: 13 July 2020 doi:10.20944/preprints202007.0274.v1

## 4.2. X-ray Diffraction

Xray diffraction studies were carried out using a Seifert XRD 3003TT$^R$ equipment, using a 2 kV - 60 kV discharge potential with a chi-arm with φ and cartesian coordinate sample manipulator. Xray diffraction θ - 2θ scans are of prime relevance to this work and were accomplished in detail. Table 6 shows the processing history of the samples subjected to Xray diffraction analysis. The sample groups in Table 6 are representative of 10 samples, each, subjected to a particular sputtering and/or annealing cycle.

| Sample | Sputtering | | | | Rapid Thermal Annealing | | | Annealing | | |
|---|---|---|---|---|---|---|---|---|---|---|
| Group No. | Working gas | Power [watt] | Temperature [°C] | Time [sec] | Working gas | Temperature [°C] | Time [sec] | Working gas | Temperature [°C] | Time [sec] |
| X-1 | Ar | 300 | RT | 1200 | Ar + $H_2$ (6%) | 800 | 60 | Ar + $H_2$ (6%) | 800 | 3600 |
| X-2 | Ar | 300 | RT | 600 | Ar | 1040 | 200 | - | - | - |
| X-3 | Ar | 300 | RT | 600 | Ar + $H_2$ (6%) | 750 | 15 | - | - | - |
| X-4 | Ar | 400 | RT | 1800 | Ar + $H_2$ (6%) | 750 | 200 | - | - | - |

Table 6: Processing history of the samples subjected to X-ray diffraction studies. For each sample group 10 samples were prepared for investigations.

(Ar: Argon gas; $H_2$: Hydrogen Gas).

## 4.3. Optical Transmission Spectroscopy

Si-deposited thin film samples were subjected to Optical Transmission Spectroscopy, in transmission mode, using a SENTECH SE 850 spectroscopic ellipsometer with the measured wavelengths in the range of 180 nm to 850 nm, corresponding to the edge of the UV region up to the starting edge of the IR region in the electromagnetic spectrum.

The entire SENTECH SE system has additional complementary systems to assess in the desired spectroscopic evaluation including a goniometer that is preset with an incidence angle from 40° to 90◦ to allow rotation of the sample in 5◦ steps. Intensities at different wavelength were obtained and normalized. Table 7 shows the processing history of the samples subjected to Optical Transmission Spectroscopy. The sample groups in Table 7 are representative of 10 samples, each, subjected to a particular sputtering and/or annealing cycle.

| Sample | Sputtering | | | | Annealing | | |
|---|---|---|---|---|---|---|---|
| Group No. | Working gas | Power [watt] | Temperature [°C] | Time [sec] | Working gas | Temperature [°C] | Time [sec] |
| OP-1 | Ar | 400 | RT | 1200 | - | - | - |
| OP-2 | Ar | 400 | RT | 1200 | Ar | 1000 | 3600 |
| OP-3 | Ar | 400 | 200 | 1200 | - | - | - |
| OP-4 | Ar | 400 | 200 | 1200 | Ar + $H_2$ (6%) | 1050 | 3600 |
| OP-5 | Ar | 400 | 200 | 1800 | Ar | 1000 | 3600 |
| OP-6 | Ar | 400 | 200 | 1800 | Ar + $H_2$ (6%) | 1000 | 3600 |
| OP-7 | Ar + $H_2$(6%) | 400 | 200 | 1800 | - | - | - |
| OP-8 | Ar + $H_2$(6%) | 400 | 200 | 1800 | Ar | 1000 | 3600 |
| OP-9 | Ar + $H_2$(6%) | 400 | 200 | 2400 | - | - | - |
| OP-10 | Ar + $H_2$(6%) | 400 | 200 | 2400 | Ar | 1000 | 3600 |

Table 7: Processing history of the samples subjected to Optical Transmission Spectroscopy. For each sample group 10 samples were prepared for investigations.

(Ar: Argon gas; $H_2$: Hydrogen Gas).

Preprints (www.preprints.org) | NOT PEER-REVIEWED | Posted: 13 July 2020 doi:10.20944/preprints202007.0274.v1

# 5. Results & Discussion

## 5.1. Raman Spectroscopy

Micro-Raman probe techniques have been prevalent to distinguish the localized crystal orientation of c-Si and a-Si. Since both these polymorphs of Si have different structural configurations, their Raman spectra exhibits different, characteristic, Raman active modes. Figure 7 shows the Raman spectra of c (single crystal)-Si, a-Si, and µ-Si [34, 35].

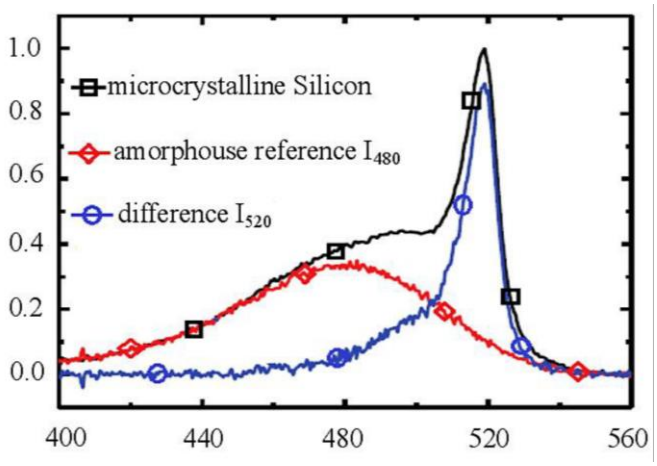


Figure 7: Characteristic Raman shifts for c-Si, a-Si, and µ-Si. [34, 35]

The Raman spectrum of c-Si is dominated by a sharp distinctive peak centered at 520 $cm^{-1}$ because of Γ`25 phonon excitation. Since the a-Si has an absence of long-range order and is characterized by a short-range translational symmetry, the quantum wave number K* is not well defined and phonon excitation occurs without the constraint of K* conservation [34]. Hence, the Raman spectra of a-Si depicts a large range of intensity distribution albeit any sharp distinctive peaks and is centered around 480 $cm^{-1}$ and 380 $cm^{-1}$ indicating the amorphous phase, the former corresponding to the excitation of transverse optical phonon and the latter to the excitation of the longitudinal optical phonon.

For µ-Si, which contains a large region of pure crystalline phases and small regions of amorphous phases, a combination of peaks of c-Si and a-Si are observed and can be seen in Figure 7. It should be noted that although Raman crystallinity is widely used as a measure of long-range order prevalent in a material, the peaks used to define it vary and it is an estimated measure of the true crystalline volume content. For the Si polymorphs, additional peaks at 500$cm^{-1}$ are often used and very frequently the peak at $I_{380}$ is disregarded [34, 35].

In this study, investigations were also made to assess the crystallinity of the as-deposited samples and post heat treated deposited samples, Table 4. Figure 8 shows a Raman spectrum of a-Si and c-Si thin films deposited at 300°C at room temperature with 300W applied for 1200s (Sample Group R-1) and at 300°C at room temperature with 300 W applied for 1200s followed by an annealing step at 800°C for 36000s (Sample Group R-2). The intensity vs. $cm^{-1}$ variation exhibits a similar behavior as is usual for an amorphous and crystalline Si with peaks centered at 480 $cm^{-1}$ and 520 $cm^{-1}$ respectively and is comparable to a standardized Raman peak observation such as in Figure 7.

Preprints (www.preprints.org) | NOT PEER-REVIEWED | Posted: 13 July 2020 doi:10.20944/preprints202007.0274.v1

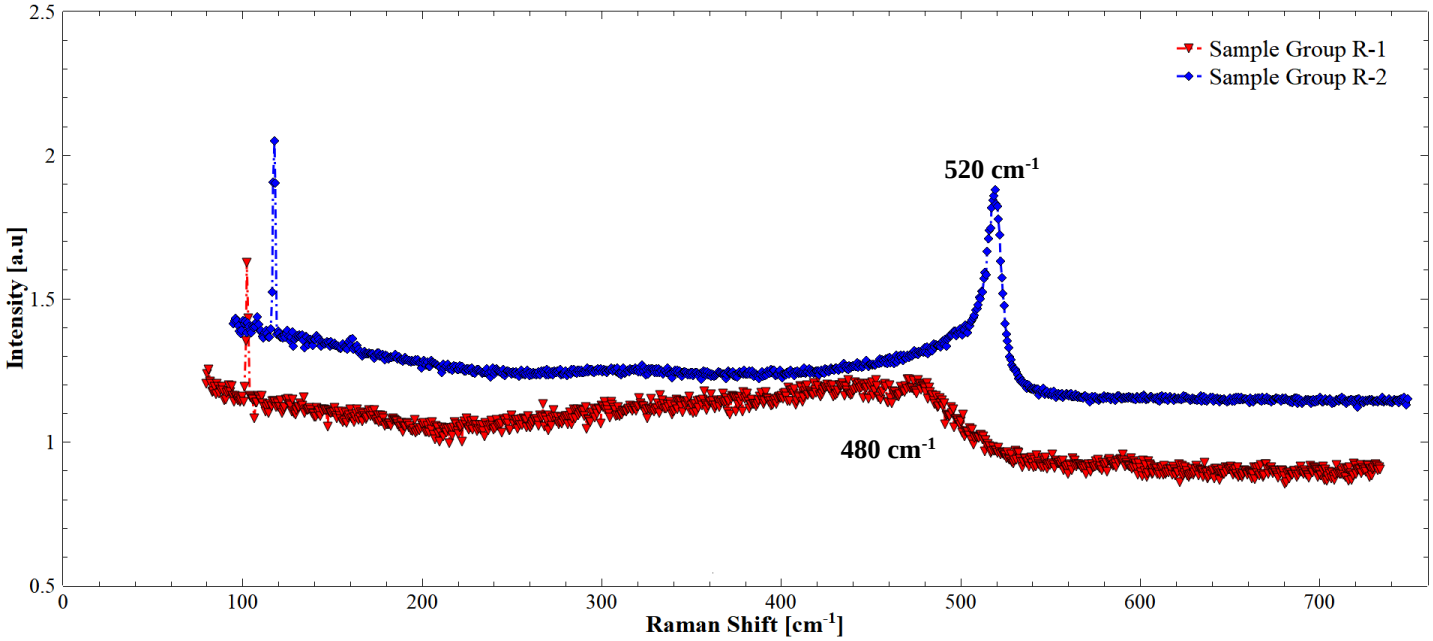


Figure 8: Characteristic Raman shifts for Sample Group R-1 (as-deposited) and Sample Group R-2 (heat treated). Sample group processing history can be viewed in Table 4.

From Figure 8, it is evident that the presence of the sharp crystalline peak and the amorphous region is highly dependent on the processing history of the deposited thin film. Sample Group R-1 (Table 4), being an as-deposited sample with no post-sputtering treatment, exhibits an amorphous Raman profile because the energy barrier required for nucleation to initiate and evolve was not overcame due to deficient energy input during the sputtering process. Sample Group R-2 (Table 4) was subjected to an annealing post treatment after sputtering, at the same deposition parameters as Sample Group R-1 (Table 4) and shows a Raman profile characteristic of a crystalline sample.

The a-Si can be characterized as Zone $I_a$ films [36], Figure 9,where adatom mobility, i.e. the n-Si atoms deposited on the substrate, is low, as a result of low energy input per incident particle and each adatom only adheres to the position on the substrate where it was initially deposited. Since no further annealing steps were carried out on Sample Group R-1 (Table 4), the energy limitations on the Si adatom produces a non-preferential crystallographic orientation and is observed as a large non-distinctive hump in Figure 8, centered around 480 $cm^{-1}$. Although the energy input per incident particle remains relatively similar to Sample Group R-1 (Table 4), Sample Group R-2 (Table 4) was subjected to an annealing step which increases the n-Si adatoms surface mobility. The resulting grain structure can be classified as Zone T [36], Figure 10, and is characterized by growth rate dependent preferential crystallographic orientation as evident by a sharp peak centered at 520 $cm^{-1}$ in Figure 8.

Preprints (www.preprints.org) | NOT PEER-REVIEWED | Posted: 13 July 2020 doi:10.20944/preprints202007.0274.v1

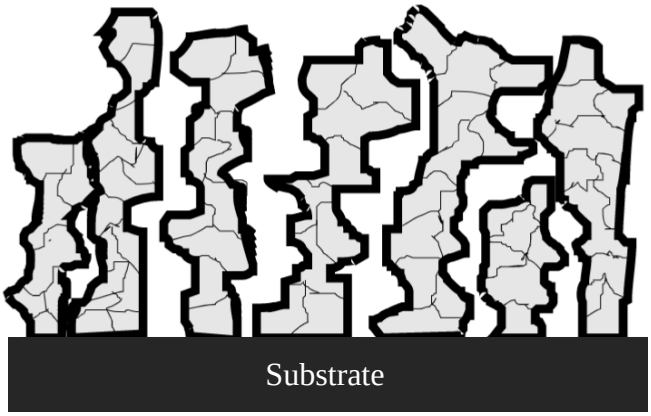


Figure 9: Zone $I_a$ thin films characterized by non-preferential crystallographic orientations due to low energy deposited atoms having minimal surface energy for re-arrangement [36].

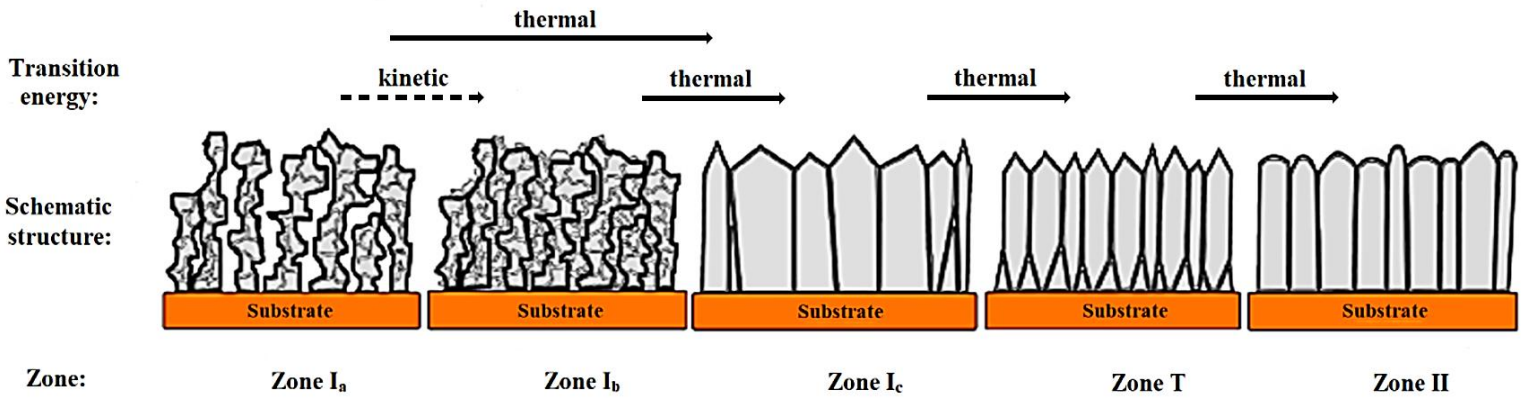


Figure 10 – Zone schemes for different energy transitions [36].

Preprints (www.preprints.org) | NOT PEER-REVIEWED | Posted: 13 July 2020 doi:10.20944/preprints202007.0274.v1

### 5.1.1. Effect of power input to the plasma during sputtering

It should be pointed out that increasing the power input to the adatoms during the sputtering has no effect on the nature of the bonding present after the sputtering process. Sputtering at 300 W and 400 W, with or without heating of the substrate during the sputtering process, resulted in an amorphous morphology as is evident in the Raman spectra in Figure 11. The samples in Figure 11 were subjected to the sputtering protocols in Table 4, without any post-sputtering heat treatment. It can thus be determined that a subsequent annealing step is necessary for the evolution of crystalline Si.

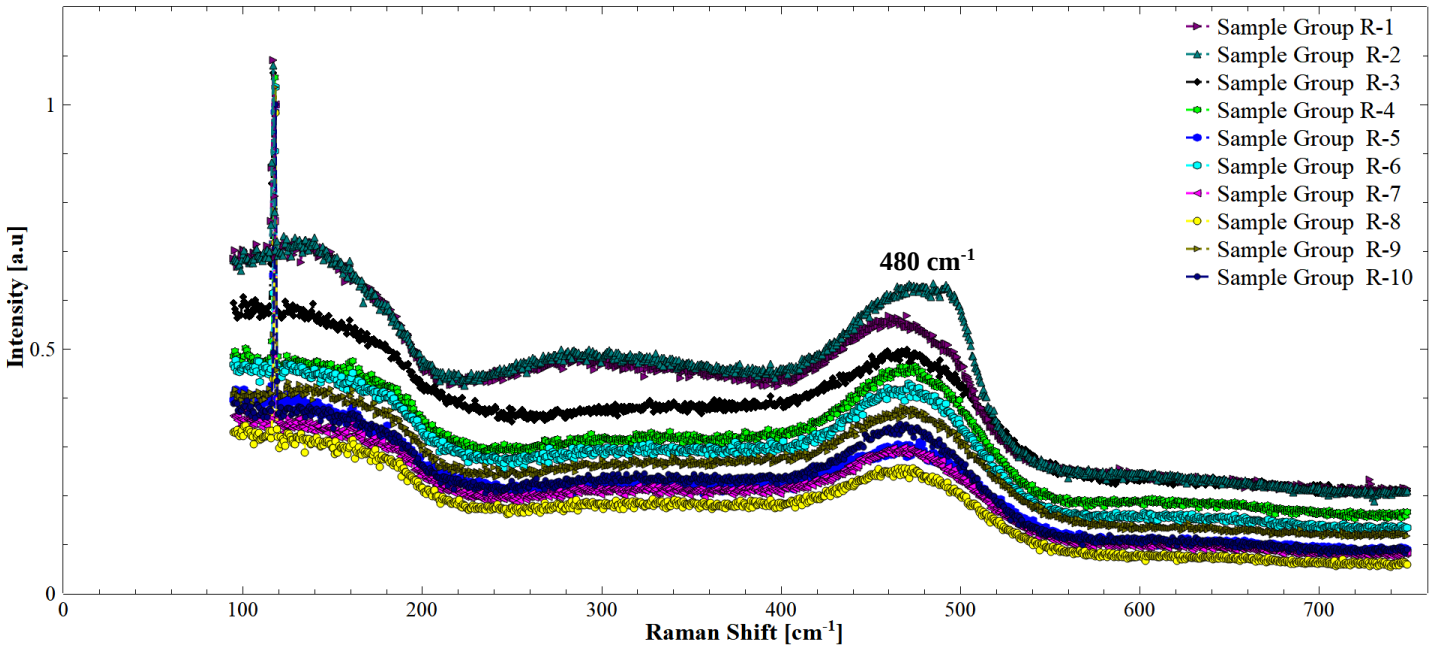


Figure 11: Effect of power input on the nature of crystallinity, during the sputtering process, predominantly amorphous, centered around 480 $cm^{-1}$. No heat treatment of the deposited n-Si thin film was carried out.

Sample group processing history can be viewed in Table 4.

Preprints (www.preprints.org) | NOT PEER-REVIEWED | Posted: 13 July 2020 doi:10.20944/preprints202007.0274.v1

### 5.1.2. Effect of substrate heating during sputtering

Heating the substrate during the deposition has no major influence on the crystallinity of the deposited Si thin film. Figure 20 shows the Raman spectra of samples from Sample Group R-3, Sample Group R-5) Sample Group R-6 and Sample Group R-8. All of these samples were sputtered at 400 W in Ar atmosphere. Sample Group R-3 was sputtered at room temperature and the rest of the samples were sputtered at 200°C (see Table 4 for processing history). These samples exhibit an amorphous region, evident by the diffuse region in the graph, Figure 12, centered at 480 $cm^{-1}$. One possible reason for this behavior can be attributed to the duration of the sputtering process. Since the deposition time was for a maximum of 2400 s for these samples, not enough energy was imparted to enhance the adatom Si surface mobility or for crystallographic orientations to be distinctive, hence indicating the need for a post-sputtering treatment to trigger the solid-state diffusion process.

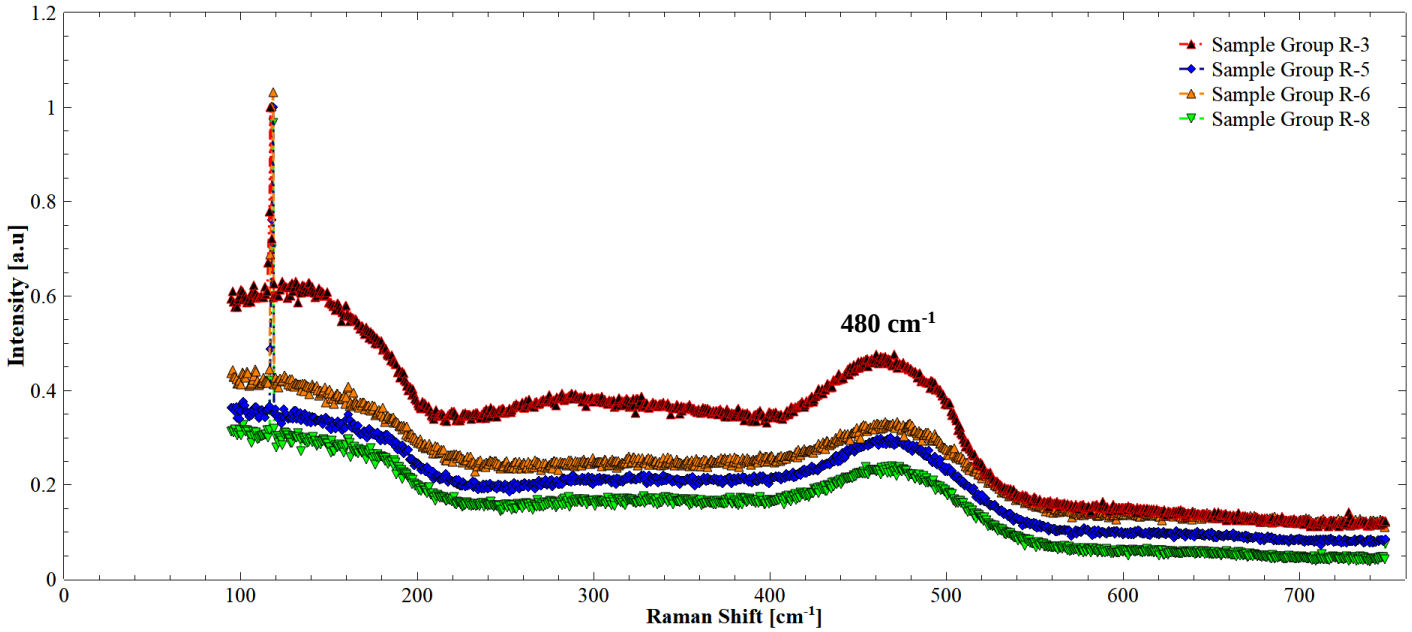


Figure 12: Effect of substrate heating on the nature of crystallinity, during the sputtering process, predominantly amorphous, centered around 480 $cm^{-1}$.

Sample group processing history can be viewed in Table 4.

Preprints (www.preprints.org) | NOT PEER-REVIEWED | Posted: 13 July 2020 doi:10.20944/preprints202007.0274.v1

### 5.1.3. Effect of post sputtering annealing on crystallinity

Figure 13 shows the Raman spectrum of Sample Group R-8-b and Sample Group R-8-c. Sample Group R-8-b was sputtered in Ar atmosphere at 200°C using 400W for 2400s and then subsequently annealed in Ar atmosphere at 1000°C for 3600s whereas Sample Group R-8-c was sputtered in Ar + $H_2$ (6%) atmosphere at 200°C using 400W for 2400s and then subsequently annealed in Ar atmosphere at 1000°C for 3600s (Table 4). Both samples differ by the nature of gas used in the annealing process.

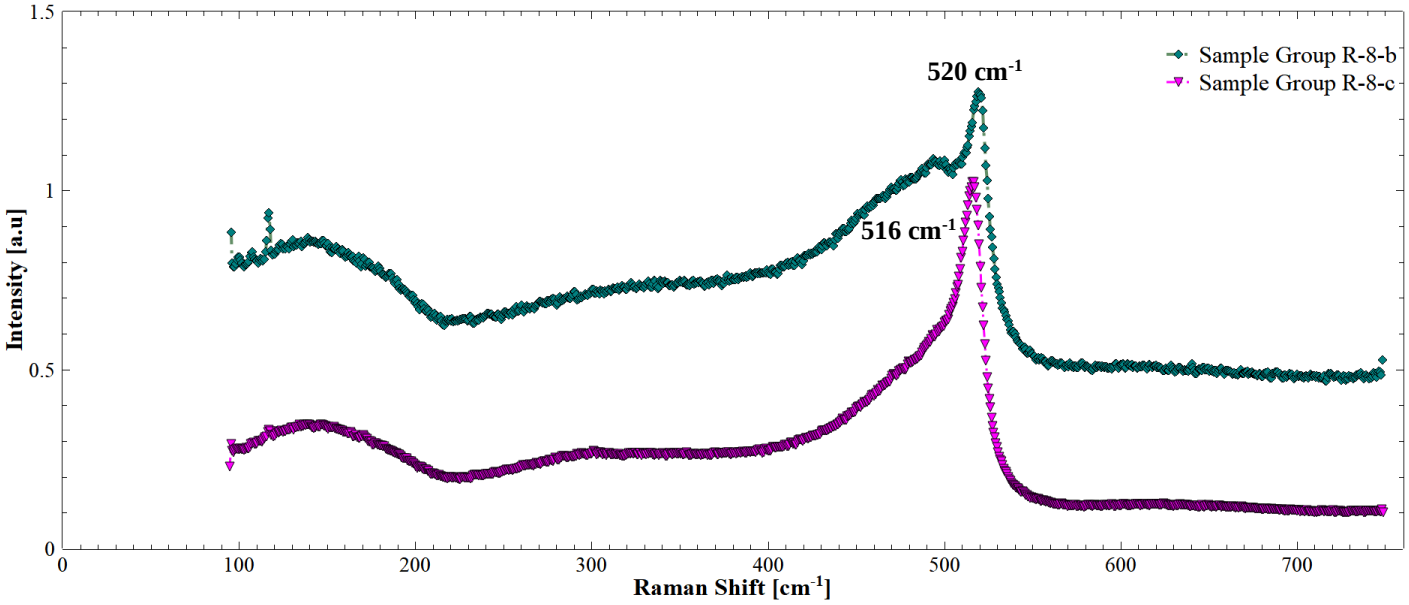


Figure 13: Effect of post sputtering annealing on the nature of crystallinity of samples sputtered in different working gas. Sharp peaks of crystallinity can be observed for Sample Group R-8-b and Sample Group R-8-c, sputtering in Ar and Ar + $H_2$ (6%) respectively.

Sample group processing history can be viewed in Table 4.

It can be observed in Figure 13 that since both samples were subsequently annealed after the sputtering process, they exhibit sharp crystalline regions, irrespective of the working gas during the sputtering process and that Sample Group R-8-b is characterized by a c-Si Raman peak at 520 $cm^{-1}$ whereas Sample Group R-8-c displays a c-Si Raman peak at 516 $cm^{-1}$.

It can be intuitively deduced that the occurrence of the sharp distinct Raman peak for Si at 520 $cm^{-1}$ occurs when all the adatoms are allowed to diffuse freely over the surface of the substrate and cooperatively contribute towards an analogous crystallographic orientation. Hydrogen gaseous species present in the plasma during the deposition process are smaller and more kinetically active as compared to Ar species. This can lead to higher occurrence of collisions between the H atoms and the Si adatoms, resulting in a relatively larger transfer of momentum, thus allowing surface adatoms to diffuse more profusely. The H gaseous species can also impart significant momentum to the substrate creating heterogeneous nucleation sites for the Si adatoms to coalesce, form stable nuclei and subsequent islands. Since the Ar atoms are much heavier, their impact on momentum transfer to the Si adatoms is comparatively lower and they have insufficient energy to create a heterogeneous nucleating environment on the substrate surface. Hence, there can be significantly large amorphous regions when Ar alone is used as a sputtering gas and these regions can contribute to a peak shift towards a lower value nearer to 480$cm^{-1}$, which is distinctive for the a-Si regime.

Preprints (www.preprints.org) | NOT PEER-REVIEWED | Posted: 13 July 2020 doi:10.20944/preprints202007.0274.v1

### 5.1.4. Effect of Ar and Ar + $H_2$ (6%) during post sputtering annealing on crystallinity

Using the Ar gas for annealing can also possibly restrain the formation of a crystalline long-range order in Silicon. To investigate the possible influence of the working gas during the post-sputtering treatment, 5 samples each, subjected to sputtering and post-sputtering treatments, were chosen from Sample Group R-5 (Table 4). For the post-sputtering treatment step, long cycle annealing treatment was preferred to allow for maximum solid-state diffusion. Figure 14 shows the effect of using Ar and Ar + $H_2$ (6%) during long cycle annealing at 1050°C for 3600s. Samples from Sample Group R-5 were sputtered at room temperature for 1800s and were then annealed at 1050°C for 3600s. Sample Group R-5-b was annealed in Ar + $H_2$ (6%), at 1050°C for 3600s, whereas Sample Group R-5-c was annealed in Ar only, at 1050°C for 3600s. Sample Group R-5-a was used as a control sample subjected only to sputtering without any post-sputtering treatment.

It can be observed Sample Group R-5-b shows a sharp crystalline peak which is in complete contrast with Sample Group R-5-c which shows an amorphous profile. This experimentally affirms the prediction that using Ar + $H_2$ (6%) as in either the sputtering or annealing stages would result in a crystalline Si morphology centered at 520 $cm^{-1}$, for reasons aforementioned.

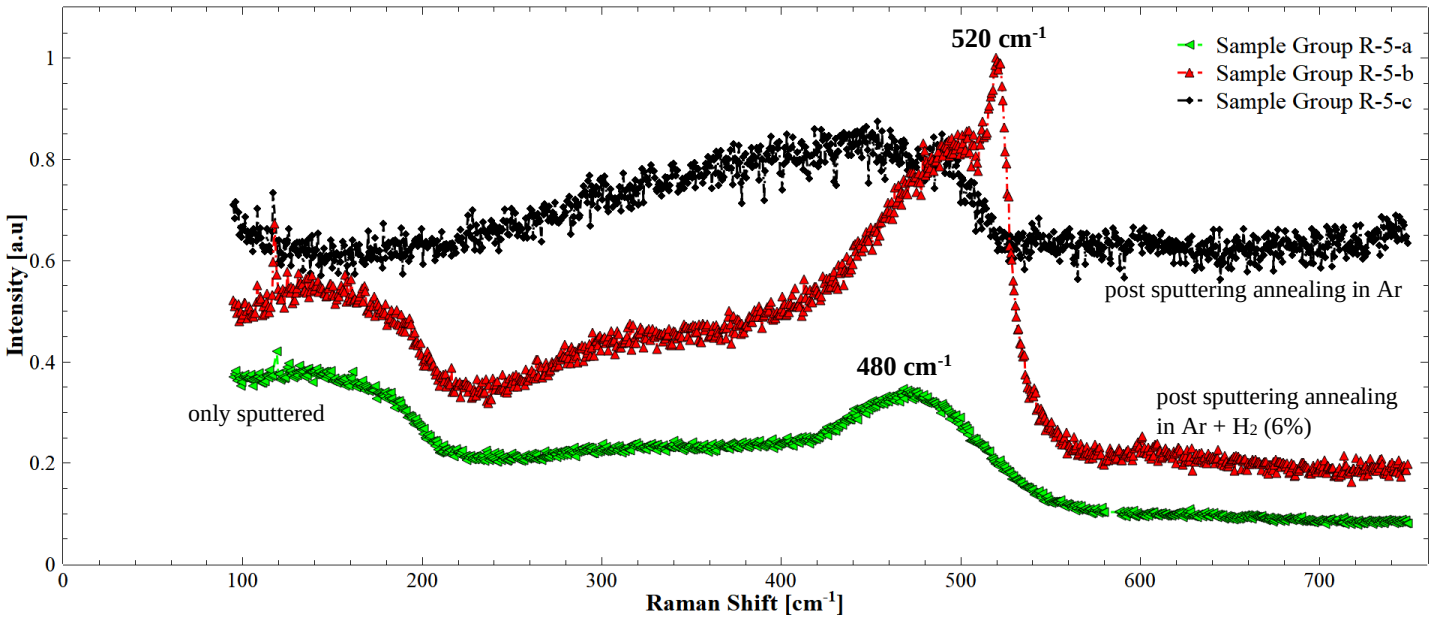


Figure 14: Effect of using different working gases, Ar and Ar + $H_2$ (6%), for post sputtering annealing on the nature of crystallinity of sputtered samples. Sharp peak of crystallinity, at 520 $cm^{-1}$, can be observed for only Sample Group R-5-b subjected to post-sputtering annealing in Ar + $H_2$ (6%) atmosphere.

Sample group processing history can be viewed in Table 4.

Preprints (www.preprints.org) | NOT PEER-REVIEWED | Posted: 13 July 2020 doi:10.20944/preprints202007.0274.v1

### 5.1.5. Investigations to ascertain optimal post-sputtering route for crystalline n-Si

Investigations were also made to ascertain the optimal post sputtering route for the formation of crystalline Silicon. Figure 15 shows the Raman spectra of Sample Group R-2-a, Sample Group R-2-b, and Sample Group R-2-c from Sample Group 2 in Table 4. All these samples were sputtered in Ar + $H_2$ (6%) environment at 300W for 1200s. Sample Group R-2-c was then subjected to a long annealing cycle for 3600s at 1000°C whereas Sample Group R-2-b was subjected to an RTA (rapid thermal annealing) cycle for 200s at 1000°C.

It is evident that the RTA process fails to crystallize the Si whereas the long cycle annealing process was more effective in generating crystallinity. This can be attributed to the conclusion that the RTA process did not provide enough time for the energy dissipation to occur through the sample, for the Si adatoms to attain the required energy for activating the crystallization process. The long annealing process, on the other hand, provided enough time for diffusion to take place. Since crystallization is dependent on nuclei formation and growth and is a diffusion-controlled process, enough time should be provided for crystallization to occur and mediate collective formation of the most energetically stable crystallographic orientation.

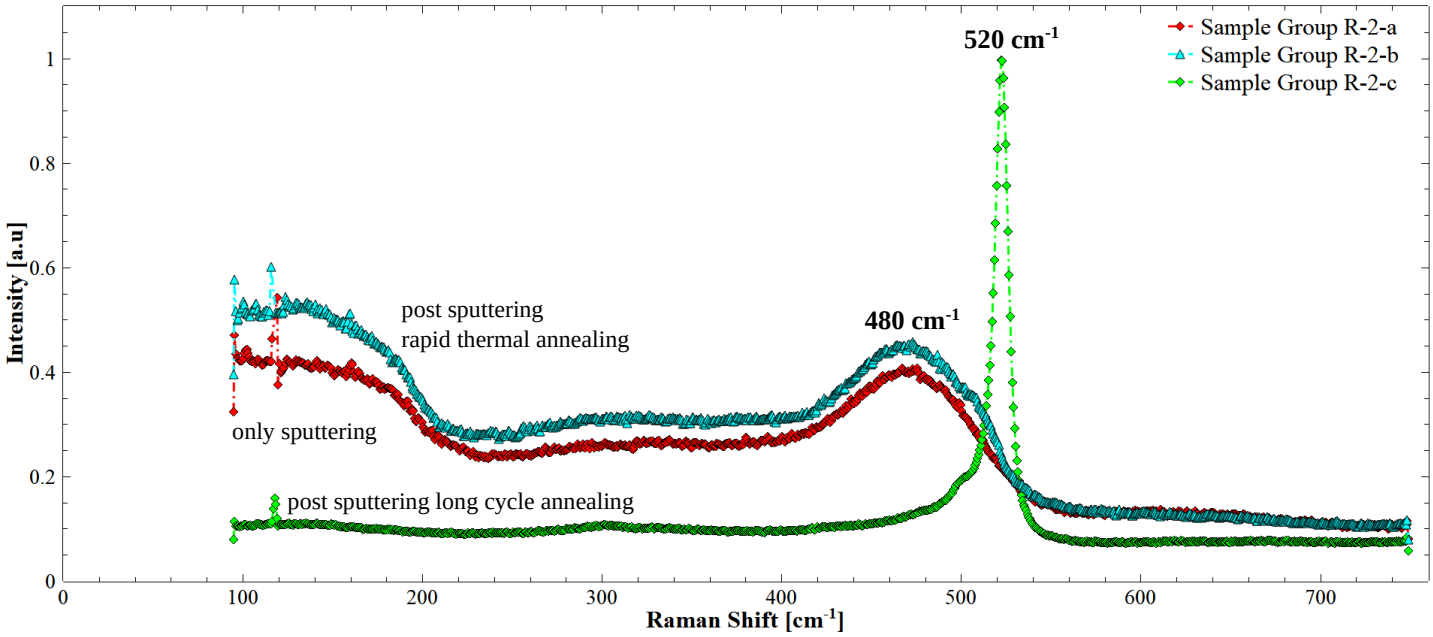


Figure 15: Effect of post sputtering processing on deposited Si under rapid thermal annealing and long cycle annealing. Sharp peak of crystallinity, at 520 $cm^{-1}$, can be observed for only Sample Group R-2-c, subjected to post-sputtering long cycle annealing.

Sample group processing history can be viewed in Table 4.

Preprints (www.preprints.org) | NOT PEER-REVIEWED | Posted: 13 July 2020 doi:10.20944/preprints202007.0274.v1

### 5.1.6. Investigations for the formation of Si:H compounds in the deposited n-Si thin films

To investigate the formation of Si-H compounds in the deposited Si thin films, localized probing through Raman Spectroscopy in the 600 $cm^{-1}$ to 2500 $cm^{-1}$ range was carried out. During the sputtering and annealing protocols, inquiries were made to ascertain the crystallinity of the deposited Si thin films by using Ar + $H_2$ (6%) gas during the process.

It is evident from the Raman spectrum that a relatively higher crystallinity is achieved by using Ar + $H_2$ (6%) as the working gas during sputtering or annealing. Si forms Si:H, Si:$H_2$ and Si:$H_3$ in the presence of $H_2$ at high temperatures, each manifesting with their own distinctive Raman signatures.

Table 5 shows the processing history of the samples subjected to Raman Si:H analysis.

Figure 16 shows the Raman spectrum of Sample Group RSH-1-a and Sample Group RSH-1-c both from Table 5. Both these samples were sputtered in Ar + $H_2$ (6%) atmosphere for 1200s at room temperature under 300W. Sample Group RSH-1-c was later subjected to an annealing protocol at 800°C in Ar atmosphere for 3600s. Both samples show Raman active peaks at the vibrational frequency of 840 $cm^{-1}$ corresponding to Si:$H_2$ implying the bending of Si:H bonds.

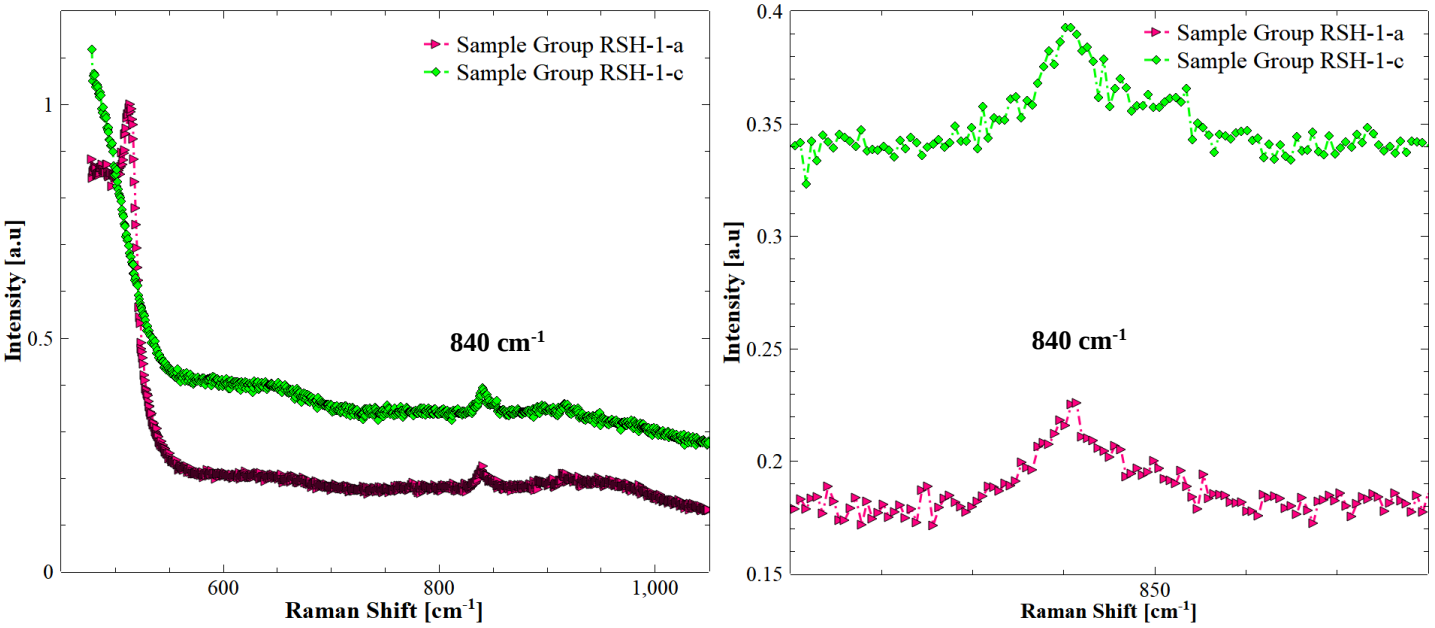


Figure 16: (a) Raman active spectrum of Si:H bonds in Sample Group RSH-1-a and Sample Group RSH-1-c in the 800 cm-1 range. (b) Enlarged localized scale between 820 $cm^{-1}$ and 880 $cm^{-1}$ for clear visibility of the Si:H Raman active peaks at the vibrational frequency of 840 $cm^{-1}$.

Sample group processing history can be viewed in Table 5.

Preprints (www.preprints.org) | NOT PEER-REVIEWED | Posted: 13 July 2020 doi:10.20944/preprints202007.0274.v1

Figure 17 shows the Raman active spectra for Sample Group RSH-1-a and Sample Group RSH-1-c in the 2000 $cm^{-1}$ range. Since Sample Group RSH-1-a is amorphous it shows a large peak at 2100 $cm^{-1}$ indicating bond stretching of Si:H and Sample Group RSH-1-c being crystalline shows a Raman active peak at 2060 $cm^{-1}$. The Raman active peak at 2060 $cm^{-1}$ for c-Si is attributed to the inner surface of a di-vacancy and a preferred assignment of the (Si:Si) $Si:H_2$ groups at the inner surfaces of the large voids [34]. It should be also mentioned that a crystalline peak at 2060 $cm^{-1}$ should be accompanied by a Raman active peak at 840 $cm^{-1}$, which is also true in this instance, and can be observed in Figure 16 for Sample Group RSH-1-a.

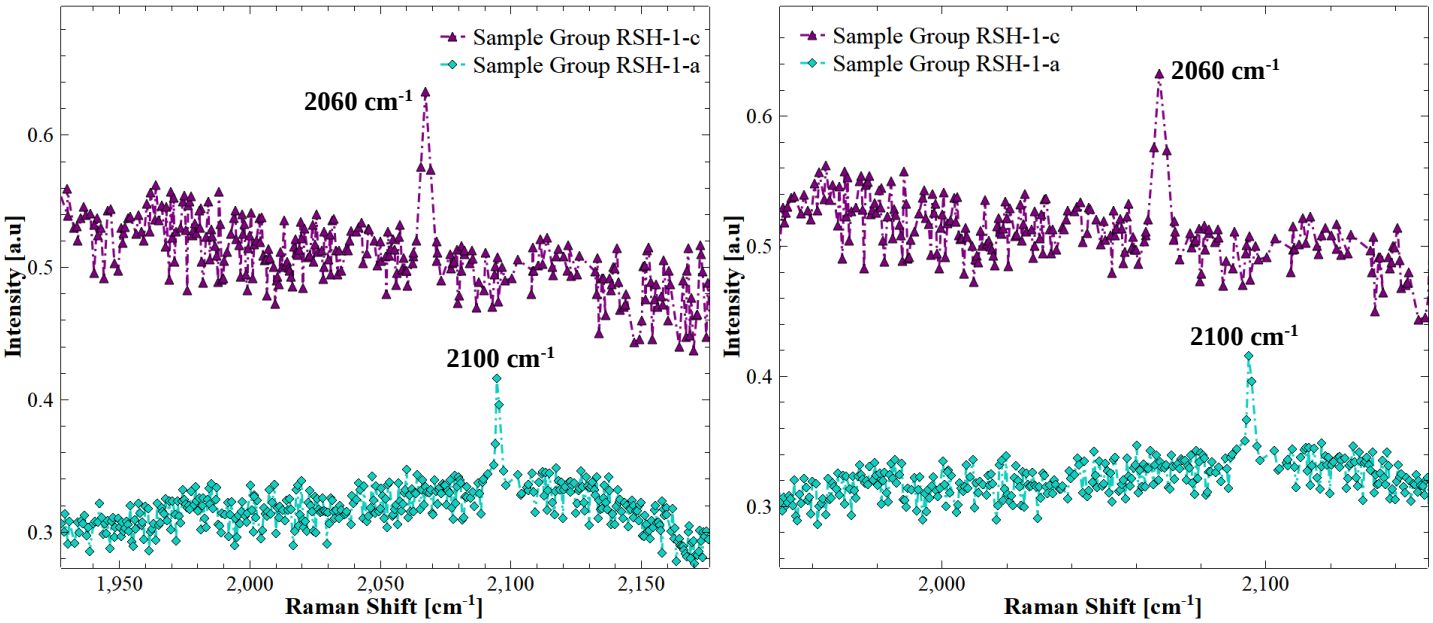


Figure 17: (a) Raman active spectrum of Si:H bonds in Sample Group RSH-1-a and Sample Group RSH-1-c in the 2000 $cm^{-1}$ range. (b) Enlarged localized scale between 1850 $cm^{-1}$ and 2200 $cm^{-1}$ for clear visibility of the Si:H Raman active peaks at the vibrational frequencies of 2060 $cm^{-1}$ and 2100 $cm^{-1}$.

Sample group processing history can be viewed in Table 5.

Preprints (www.preprints.org) | NOT PEER-REVIEWED | Posted: 13 July 2020 doi:10.20944/preprints202007.0274.v1

## 5.2. X-Ray Diffraction

The XRD analysis on the samples in this current work was carried out to ascertain the long- or short-range order prevalent, as a consequence of the sample's processing history. Since XRD gives distinct sharp peaks for a crystalline material and a large non-distinct hump for an amorphous material, this technique, in tandem with Raman spectroscopy, was considered relevant to provide a qualitative appreciation of the degree of crystallinity in the samples. Ideally speaking, crystalline Silicon has sharp peaks at 28˚ and 69˚corresponding to the planes (111) and (100) respectively [24, 32, 34].

Figure 18 shows the XRD spectrum of Sample Group R-X-1 from Table 6 subjected to both rapid thermal annealing (RTA) and long cycle annealing. The sample was initially sputtered in Ar at 300W for 1200s at room temperature. It was then subjected to an RTA treatment at 800ºC in Ar + $H_2$ (6%) atmosphere for 60s and then subsequently annealed at 800ºC in Ar atmosphere for 3600s. XRD investigations were carried out both after rapid thermal annealing and long cycle annealing. It was previously demonstrated in the section 5.1 that the Raman spectroscopy of the samples subjected to only an RTA treatment exhibit an amorphous behavior which is established further by the XRD spectra in Figure 18.

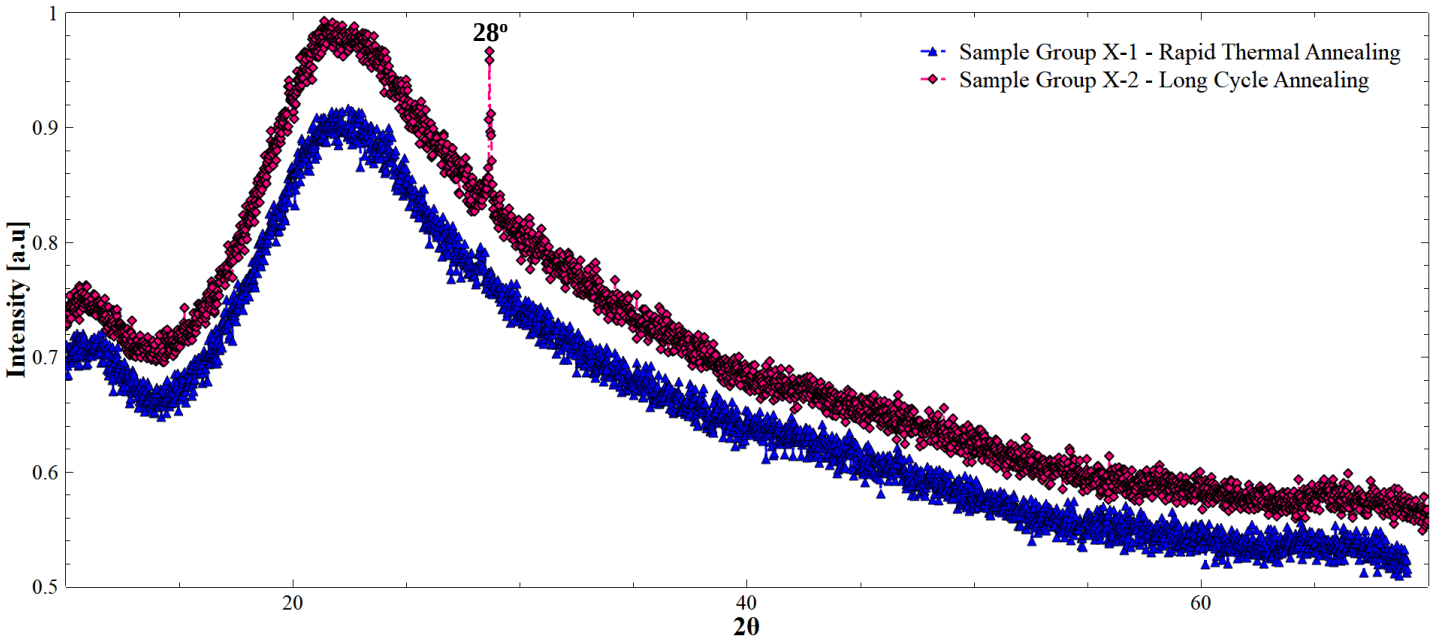


Figure 18: XRD spectrum of Sample Group X-1 after Rapid Thermal Annealing (RTA) and Long Cycle Annealing (AN). A sharp peak can be observed at 28º, for the Long Cycle Annealing (AN) post sputtering treatment, which is characteristic for c-Si.

Sample processing history can be viewed in Table 6.

Preprints (www.preprints.org) | NOT PEER-REVIEWED | Posted: 13 July 2020 doi:10.20944/preprints202007.0274.v1

Sample Group X-1 (Table 6) shows an amorphous characteristic after undergoing an RTA treatment and a crystalline characteristic after the annealing treatment. This validates the notion that a longer time duration is required for the diffusion of Si adatoms on the substrate's surface to enable the growth of crystalline Si film. This is further shown in Figure 19 which shows the XRD spectrum of Sample Group X-3 and Sample Group X-4. Both these sample groups were sputtered at 300°C for 600s at room temperature and were subjected to RTA treatment in Ar + $H_2$ (6%) atmosphere at 750°C for 15s and 200s, respectively. They both exhibit an amorphous characteristic as is expected from samples undergoing only the RTA treatment.

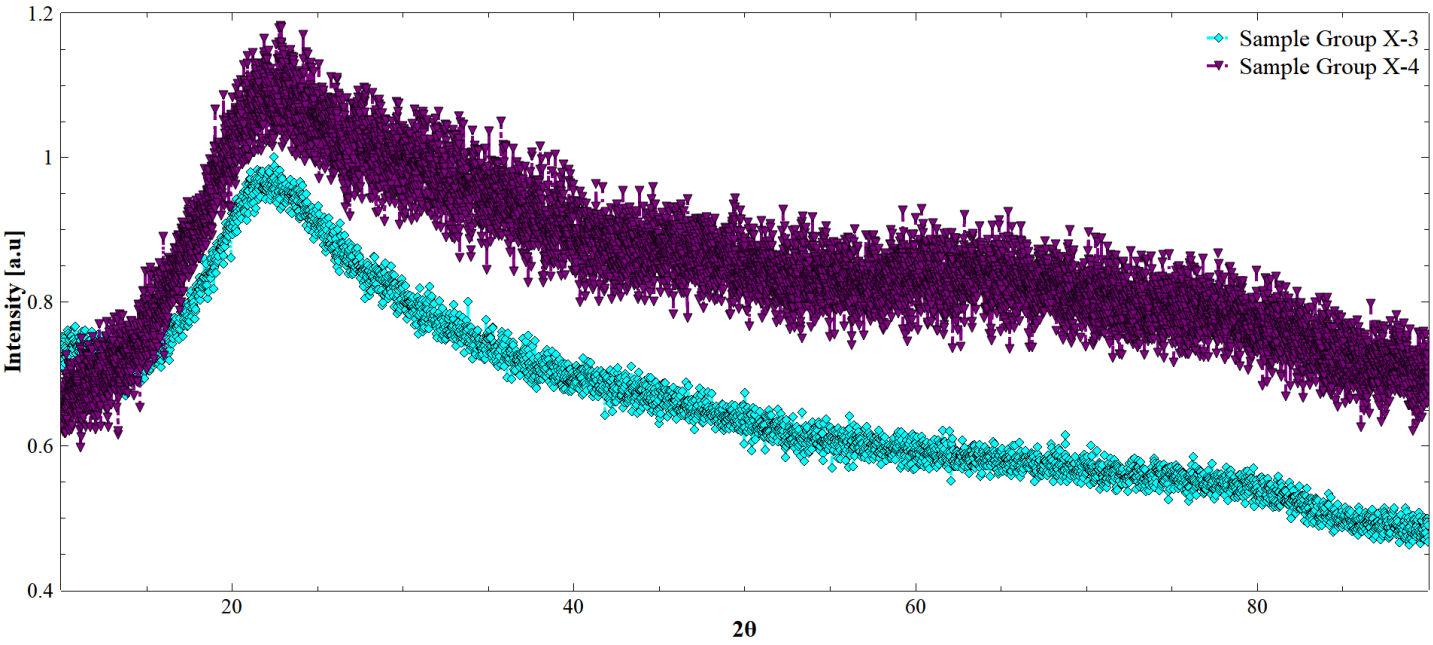


Figure 19: XRD spectrum of Sample Group X-3 and Sample Group X-4 after post-sputtering rapid thermal annealing (RTA).

Sample processing history can be viewed in Table 6.

Preprints (www.preprints.org) | NOT PEER-REVIEWED | Posted: 13 July 2020 doi:10.20944/preprints202007.0274.v1

## 5.3. Optical Transmission Spectroscopy

### 5.3.1. Effect of post sputtering treatments on transmission properties of sputtered Si

Figure 20 shows the graph of Sample Group OP-3 and Sample Group OP-4 (Table 7). Sample Group OP-3 was sputtered in Ar atmosphere for 1200s using 400W at 200°C whereas Sample Group OP-4 underwent the same sputtering treatment with an additional annealing protocol in Ar + $H_2$(6%) gas for 3600s at 1050°C. The high signal to noise ratio is due to the geometric interference of the sample's geometry and does not influence the significance of the data.

It can be observed that high transmission peaks are observed in the 700 nm - 900 nm region. This is suggestive of a higher transmission of photonic energy incident to the sample. Very low absorbance occurs indicating that the Sample Group OP-3 is has low percentage of Si present. Since this sample was annealed at a high temperature of 1050°C, it can be deduced that much of the Si has been evaporated from the substrate. The Raman spectra of Sample Group OP-4, Figure 21, concurs that the sample is indeed amorphous; characteristic of the amorphous $SiO_2$ substrate.

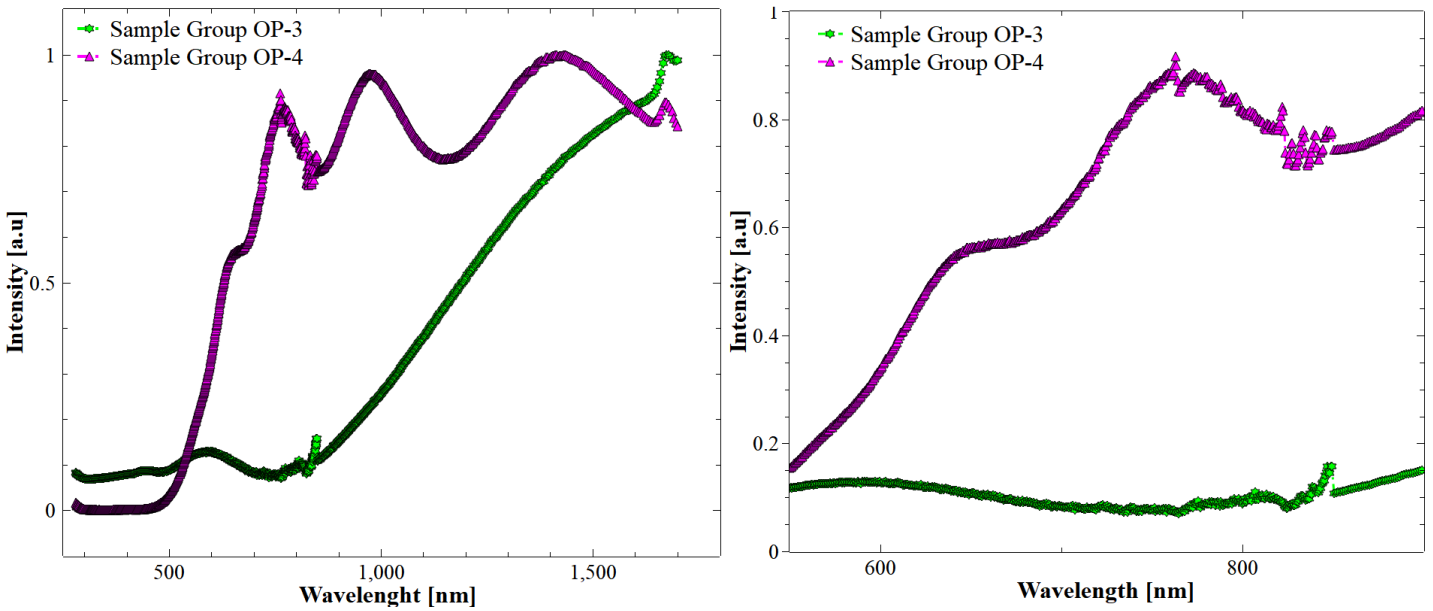


Figure 20: (a) Optical transmission of Sample Group OP-3 and Sample Group OP-4 after sputtering and long cycle annealing. Appreciable transmission peaks are evident between 700 nm - 900 nm. (b) Enlarged localized scale between 700 nm and 900 nm for clear visibility.

Sample processing history can be viewed in Table 7.

Preprints (www.preprints.org) | NOT PEER-REVIEWED | Posted: 13 July 2020 doi:10.20944/preprints202007.0274.v1

Sample Group OP-3 was only sputtered and thus was able to preserve most of the Si deposited on the substrate. The graph indicates a comparatively lower transmission percentage suggesting that Si is still deposited on the sample post sputtering.

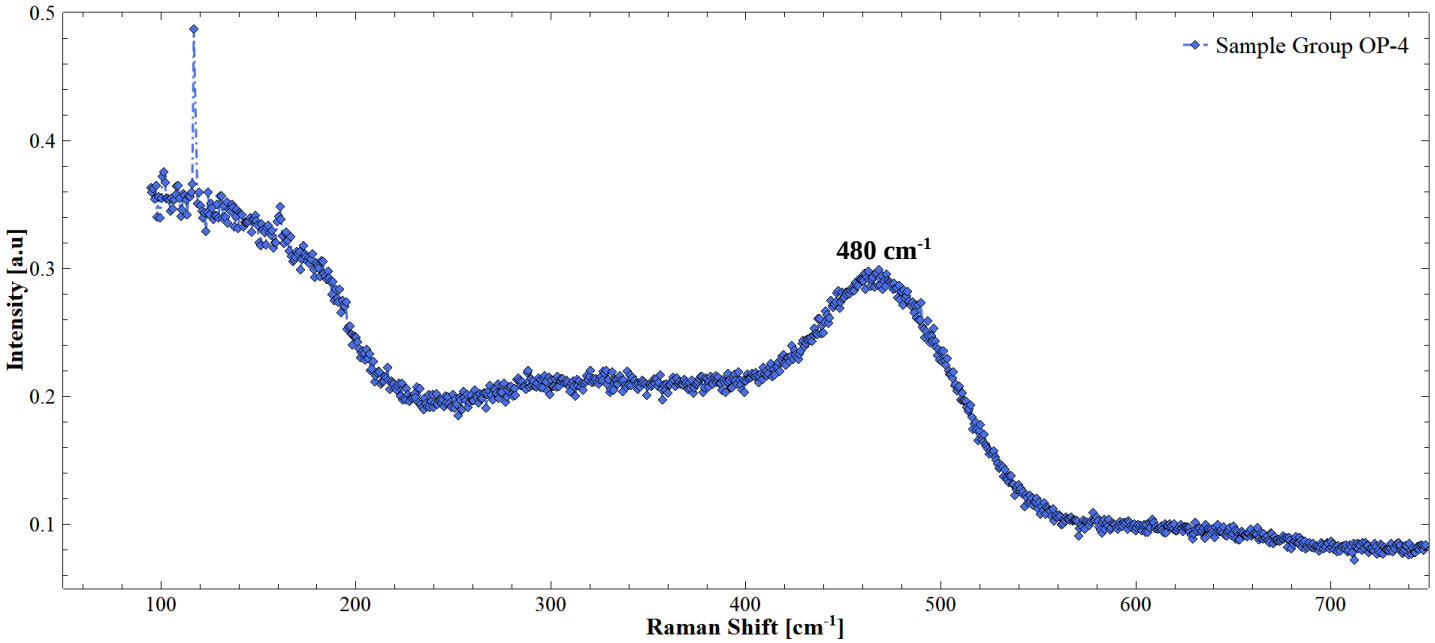


Figure 21: Raman spectra of Sample Group OP-4 (Table7) exhibiting an amorphous hump centered at 480 $cm^{-1}$.

Sample processing history can be viewed in Table 7.

To further investigate whether prolonged annealing has any effect on the optical properties of deposited n-Si, Sample Group OP-7 (Table 7) and Sample Group OP-8 (Table 7) were both sputtered at 200$^{o}$C in Ar + $H_2$(6%) atmosphere at 400W for 1800s. Sample Group OP-8 was then annealed in Ar atmosphere for 3600s. Both samples exhibit large transmission peaks in the 700 nm - 900 nm region, Figure 22, although the intensity of the transmission is larger for the annealed sample as compared to the as-sputtered sample. This indicates that the long cycle annealing may result in the loss of deposited Si from the substrate. It should be conclusively observed that if the Raman spectra indicates that a sample is amorphous, large transmission peaks are normally observed.

Preprints (www.preprints.org) | NOT PEER-REVIEWED | Posted: 13 July 2020 doi:10.20944/preprints202007.0274.v1

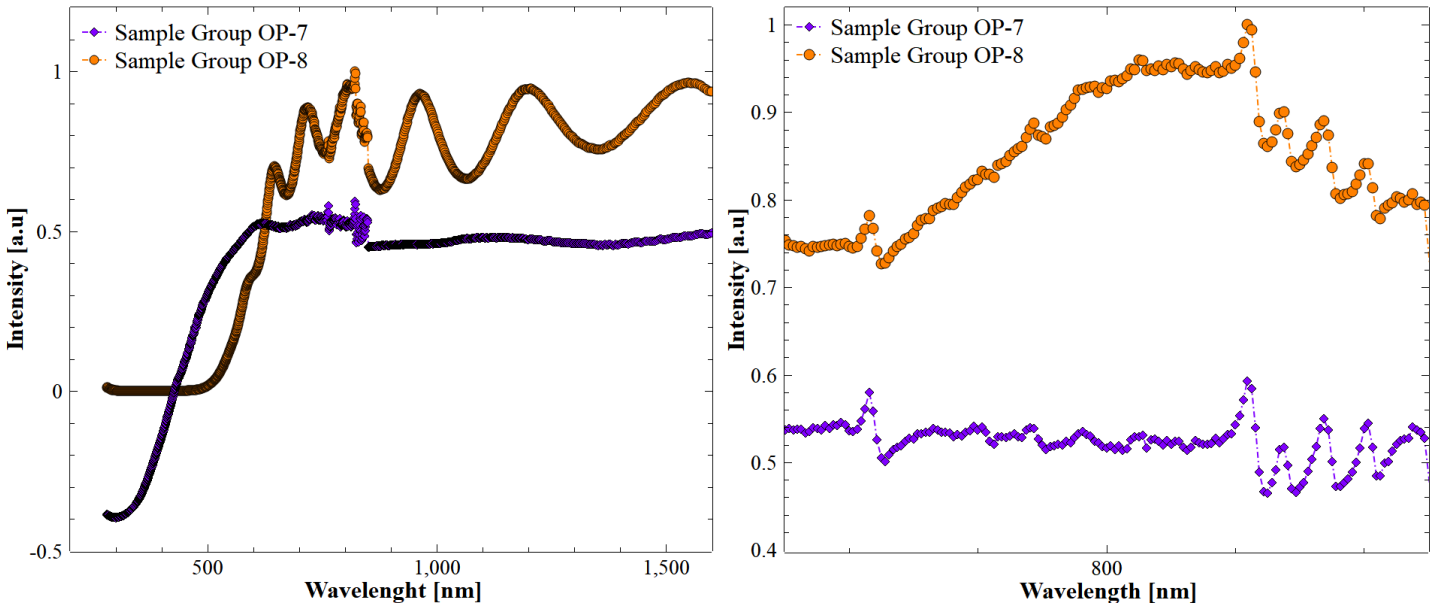


Figure 22: (a) Optical transmission spectrum of Sample Group OP-7 and Sample Group OP-8 (Table 7). (b) Enlarged localized scale between 700 nm and 900 nm for clear visibility in the desired spectrum range.

Sample group processing history can be viewed in Table 7.

Preprints (www.preprints.org) | NOT PEER-REVIEWED | Posted: 13 July 2020 doi:10.20944/preprints202007.0274.v1

### 5.3.2. Optical band gap investigations

To investigate the optical band gap from the transmission raw data at different wavelengths, the Tauc equation [38], used. Three different group of samples were compared (10 samples each), and their band gaps were related to their processing history. Sample Group OP-7 and Sample Group OP-8 (Table 7) were both sputtered in Ar + $H_2$ (6%) atmosphere at 400W for 1800s. Sample Group OP-8 was then subjected to an annealing treatment in Ar atmosphere for 3600s at 1000$^o$C.

Figure 23 shows the $(\alpha hv)^{1/2}$ vs eV plot of Sample Group OP-7 and Sample Group OP-8 (Table 7). The as-sputtered Sample Group OP-7 exhibits a band gap at 1.78eV whereas the annealed Sample Group OP-8 shows a band gap at 2.25eV. The annealing treatment, apparently, increases the percentage of the crystalline regions in the sample and leads to a higher absorption of solar spectrum as compared to the as sputtered sample.

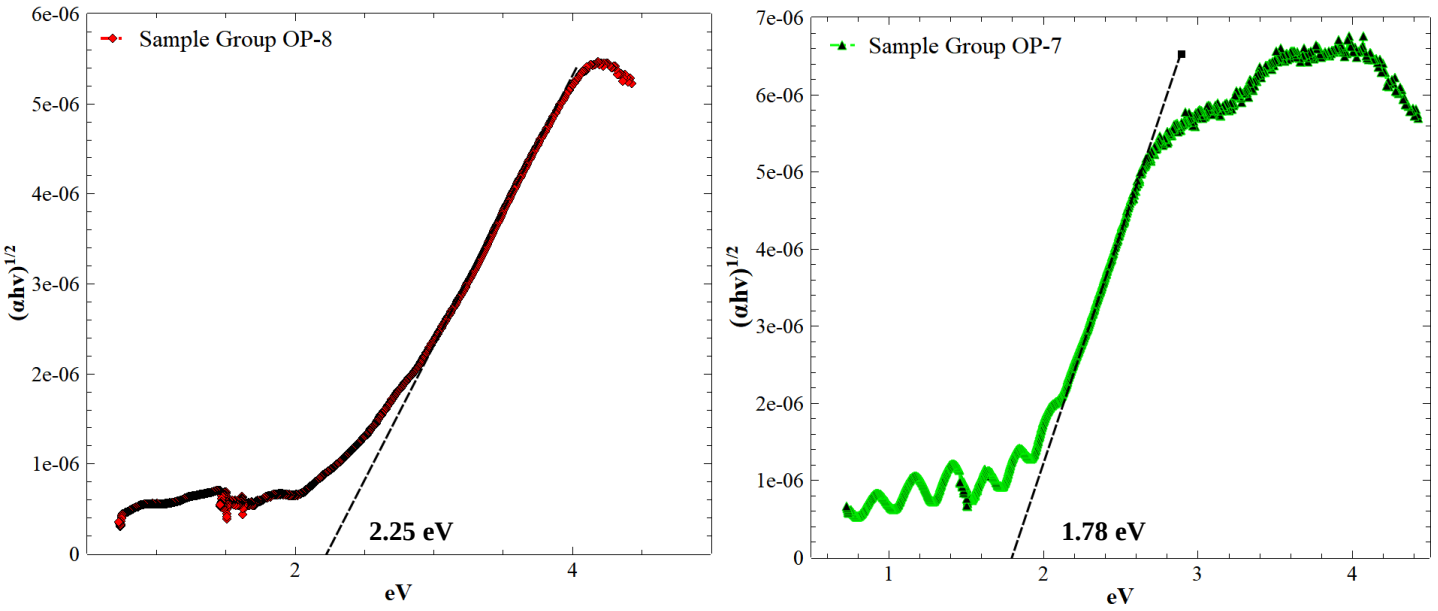


Figure 23: Optical band gap calculation using the Tauc Equation for (a) Sample Group OP-8 (b) Sample Group OP-7

Sample group processing history can be viewed in Table 7.

This observation of a higher calculated band gap in annealed samples can also be observed in other Sample Groups (100 samples, 10 each for each Sample Group) prepared in the course of the present work. Sample Group OP-1 and Sample Group OP-2 (Table 7) were both sputtered in Ar atmosphere in room temperature for 1200s at 400W. Sample Group OP-2 was further annealed in Ar at 1000$^o$C for 3600s. Figure 24 depicts their calculated band gap through the Tauc plot. The as-sputtered sample 1 shows a lower band gap at 1.8eV whereas the annealed sample 2 shows a higher band gap at 2.24eV.

Further investigations on Sample Group OP-9 and Sample Group OP-10 (Table 7) replicates the same observation. Both samples were sputtered in Ar + $H_2$ (6%) atmosphere at 200$^o$C for 2400s at 400W. Sample Group OP-10 was further annealed at 1000$^o$C for 3600s in Ar atmosphere. Figure 25 shows that the as-sputtered Sample Group OP-9 has a band gap at 1.65eV whereas the annealed Sample Group OP-10 has a higher band gap at 1.925 eV.

Preprints (www.preprints.org) | NOT PEER-REVIEWED | Posted: 13 July 2020 doi:10.20944/preprints202007.0274.v1

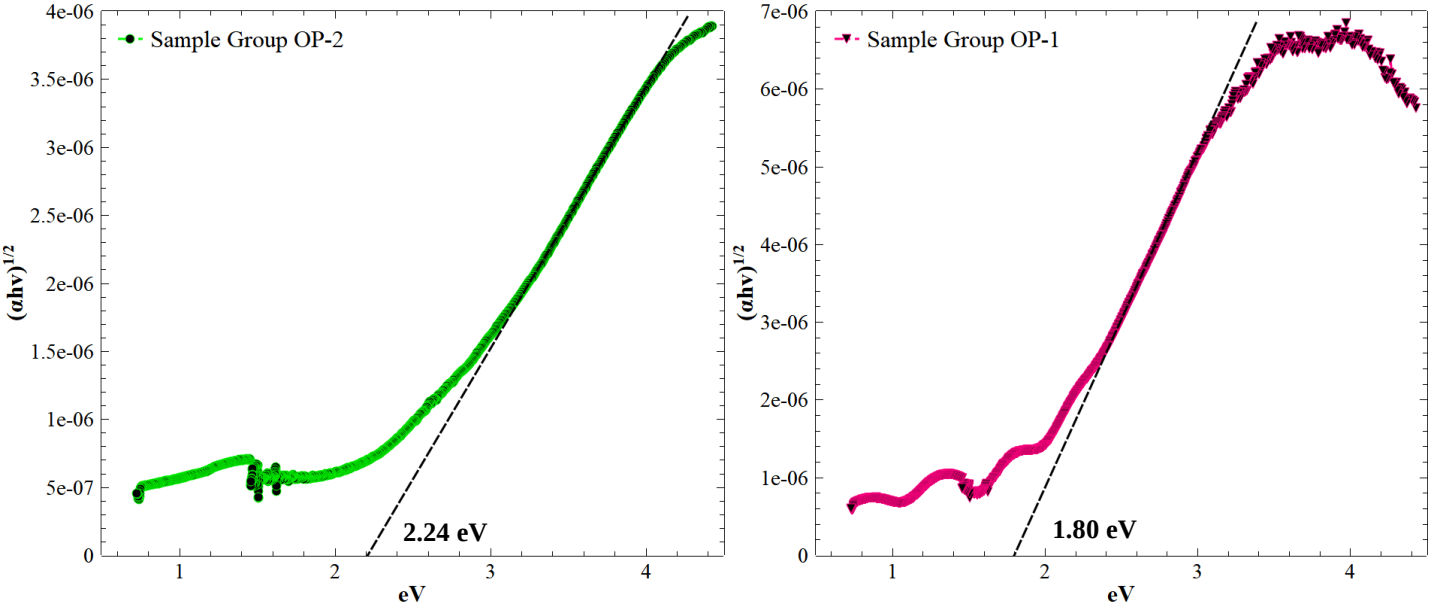


Figure 24: Optical band gap calculation using the Tauc Equation for (a) Sample Group OP-2 (b) Sample Group OP-1

Sample group processing history can be viewed in Table 7.

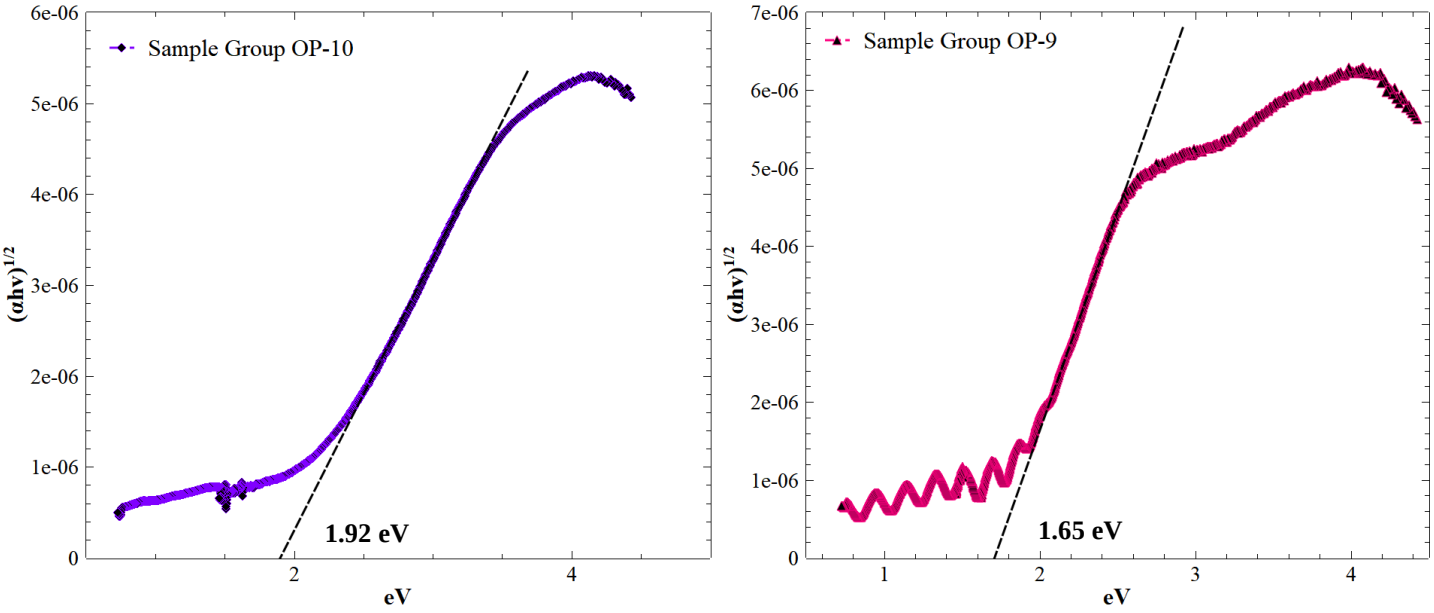


Figure 25: Optical band gap calculation using the Tauc Equation for (a) Sample Group OP-10 (b) Sample Group OP-9

Sample group processing history can be viewed in Table 7.

Preprints (www.preprints.org) | NOT PEER-REVIEWED | Posted: 13 July 2020 doi:10.20944/preprints202007.0274.v1

# 6. Conclusion

The objective of this work was to investigate the optimal conditions for the sputtering of crystalline Silicon using as low temperatures as possible yet maintaining appreciable crystallinity, adhesion and an increased or comparable theoretical optical property of the deposited film. Magnetron sputtering was decided upon as the deposition technique to deposit the Si thin films and investigations were made by varying the operating variables of the sputtering technique. Post processing of the sputtered thin films in terms of rapid thermal annealing (RTA) and long cycle annealing (AN) was carried out and their operating parameters varied to acquire a crystalline morphology of the deposited Si film.

Sputtering was carried out at 300W and 400W with different times from 600s to 2400s under Ar and Ar + $H_2$ (6%) working gas atmosphere at room temperature and at 200 $^oC$. Investigations were made through Raman spectroscopy and X-ray diffraction to ascertain whether the sputtering process alone was sufficient to cause deposition of crystalline Si thin films. It is shown in Section 5.1 and 5.2 that sputtering alone was insufficient to cause appreciable crystallinity of deposited Si thin films. The deposited thin films remain amorphous whether the deposition was carried out a 300W or if an increase in power to 400W was applied to the sputtering system, Figure 11, implying that the deposited surface Si adatoms possess insufficient mobility to form a crystalline network. These amorphous films were all congregated uniformly at a Raman active peak of 480 $cm^{-1}$, typical for a-Si. Further investigations revealed that sputtering alone by varying the deposition temperatures between RT and 200$^oC$ produced similar results, Figure 12, with a-Si being registered in the Raman analysis. A further post sputtering step like Rapid Thermal Annealing (RTA) or Long Cycle Annealing (AN) produced µc-Si, Figure 14. It was also apparent that the working gas has an appreciable effect on the occurrence of the Raman active peaks. Using Ar + $H_2$ as the working gas, exhibited the Raman active peak for µc-Si at 520 $cm^{-1}$ which is atypical for Si [34], Figure 13. There is also an indication, Figure 14, that using Ar only as a working gas either in the sputtering or post sputtering process can result in an amorphous region to manifest.

Also, a comparison between the two post sputtering processes, namely RTA and AN, lead to the conclusion that AN is preferably more prone to produce a wholly crystalline structure as compared to RTA as can be seen in Figure 15. This effect is more pronounced in the XRD analysis in Figure 18, where analysis was carried out after rapid thermal annealing and long cycle annealing. The XRD spectrum shows an amorphous profile after the RTA process whereas it shows a sharp crystalline peak at 28$^o$, characteristic for crystalline Si, for the AN process, thus confirming that the AN process is much more effecting in producing a crystalline long range order in the deposited Si thin films.

Investigations made to ascertain the occurrence of Raman active peaks for Si:H compounds indicated that whether the sample is as sputtered or is subjected to an annealing treatment, Si:H active peaks are clearly visibility at the vibrational frequency of 840 $cm^{-1}$, indicating the formation of Si:H inclusions, Figure 16. The difference in characteristic Raman active vibrational frequencies occur, at higher frequencies, if the samples is crystalline or amorphous as evident by Figure 17. The only-sputtered samples, being amorphous exhibited a large peak at 2100 $cm^{-1}$ indicating bond stretching of Si:H and the post-sputtered annealed samples, being crystalline demonstrated a Raman active peak at 2060 $cm^{-1}$. Further deduction that the as-sputtered samples were amorphous is indicated by the accompanying Raman active peak at 840$cm^{-1}$.

Optical transmission spectroscopy investigations were made to investigate if appreciable quantity of Si remained after the post sputtering processes and to determine the band gap of different samples subjected to sputtering and post-sputtering treatments. Figure 20 and 22 showed that the samples subjected to a post sputtering treatment demonstrate appreciable transmission regions between 700 - 900 nm suggesting that significant Si is lost during the post sputtering treatment. It is thus strongly urged that a post sputtering treatment should not exceed 900 $^oC$ to preserve the deposited Si.

To calculate the band gap, the Tauc equation was modified and extrapolated into a linear regression to ascertain the band gap energy. Investigations revealed that for samples subjected to a post sputtering treatment the band gap energy increased appreciably, Figures 21, 22, 23. This indicates that a post sputtering treatment produces a crystalline 3-dimensional order and is able to absorb a large range of eV as compared to only as-sputtered samples.

The present work suggests that in order to fabricate crystalline Si thin films, the important processing variable is the post sputtering treatment, preferably long cycle annealing under Ar + $H_2$ (6%) working gas atmosphere, using temperatures up to 900 $^oC$, to restrain the loss of Si at higher annealing temperatures. This study also concludes that since the long-range order formed in these samples at low temperatures is micro-crystalline, Raman spectroscopy is much more efficient and competent to assess the degree of crystallinity present in the samples as compared to XRD. It is also suggested that doing a line profile analysis of the extent of H profusion in the deposited thin film should be quantified by Elastic Recoil Diffraction Analysis (ERDA). This quantification can judge the H content of the sample to precisely engineer the optical band gap of the deposited thin film.

## Acknowledgements

The authors would like to acknowledge the excellent help, availability, and support of the technical staff at Forschungzentrum Jülich where this research project was conducted. We are particularly grateful to the members of the Peter Grünberg Institute 4 at Forschungzentrum Jülich, specially Dr. Alexander Weber, for always ready advice and thoughtful suggestions.

## Data Transparency

The authors have made the raw and analyzed data for this project available on Mendeley Data. The data set is entitled ‘Data pertaining to Si deposition via magnetron sputtering for photocatalytic conversion of water-A7-TUD’ and can be accessed with the DOI: 10.17632/g959zz7bb2.3 (http://dx.doi.org/10.17632/g959zz7bb2.3).

 doi:10.20944/preprints202007.0274.v1

# References


1. Kenichi Honda. *Electrochemical Photolysis of Water at a Semiconductor Electrode. Nature*. 1972 (28).

2. Meng Ni et al. *A review and recent developments in photocatalytic water-splitting using $TiO_2$ for hydrogen production*. Renewable and Sustainable Energy Reviews. 2007 (11); 401 - 425

3. Chi-Hung Liao et al. *Hydrogen Production from Semiconductor-based Photocatalysis via Water Splitting*. Catalysts. 2012 (2); 490 - 516

4. Qi Chen et al. *Tandem photoelectrochemical cells for solar water splitting*. Advances in Physics: X. 2018 (3:1); 1487267

5. Rengui Li et al. *Photocatalytic Water Splitting on Semiconductor-Based Photocatalysts. Advances in Catalysis*. 2017 (60)

6. Tahereh Jafari et al. *Photocatalytic Water Splitting - The Untamed Dream: A Review of Recent Advances.* Molecules. 2016 (21); 900

7. Juan Carlos Colmenares, Yi-Jun Xu. *Heterogeneous Photocatalysis: From Fundamentals to Green Applications*. Springer. 2016. ISBN 978-3-662-48719-8

8. Frank E. Osterloh. *Inorganic Materials as Catalysts for Photochemical Splitting of Water.* Chem. Mater. 2008(20); 35 - 54

9. Zhao J et al. *19.8% efficient "honeycomb" textured multi-crystalline and 24.4% monocrystalline silicon solar cells*. Applied Physics Letters. 1998 (73); 1991 - 1993

10. Joost Manassen. *Electrochemical, solid state, photochemical and technological aspects of photochemical energy converters*. Nature. 1976 (263)

11. Butler, M. A. *Photo-electrolysis, and physical properties of the semiconducting electrode $WO_2$*. Journal of Applied Physics. 1977 (48); 5; 1914-1920.

12. Tayebeh Ameri et.al. *Organic tandem solar cells: A review.* Energy Environ. Sci. 2009(2); 347 - 363

13. Thomas Kraus. *Nano-platelet cells for photoelectrochemical (PEC) water splitting and environmental applications*. Lehrstuhl für Experimentalphysik IV. University of Augsburg. 2013 (PhD Thesis)

14. Yasumichi Matsumoto. *Energy Positions of Oxide Semiconductors and Photo-catalysis with Iron Complex Oxides. Journal of Solid-State Chemistry*. 1996 (126); 2; 227 - 234

15. A. J. Bard et al. *Terminology in semiconductor electrochemistry and photo-electrochemical energy conversion, Pure & Applied Chemistry*. 1991 (63); 4; 569 - 596

16. L. Houben. *Plasmaabscheidung von mikrokristallinem Silizium: Merkmale der Mikrostruktur und deren Deutung im Sinne von Wachstumsvorgängen*. Heinrich-Heine-Universität Düsseldorf. 1998 (PhD Thesis)

17. Zuo Zewen et.al. *Growth and microstructure properties of microcrystalline silicon films deposited using ICPCVD*. Journal of Semiconductors. 2011 (32); 3

18. E. Vallat-Sauvain et.al. *Advances in Microcrystalline Silicon Solar Cell Technologies*. Thin Film Solar Cells. 2005. Wiley

19. R.B. Bergmann. *Crystalline Si thin-film solar cells: A Review*. Applied Physics A. 1999 (69); 2; 187 - 194

20. T. Sasaki et.al. *Deposition of microcrystalline silicon by electron beam excited plasma*. Solar Energy Materials and Solar Cells. 1997 (49); 81

21. M. B. Schubert. *Low temperature silicon deposition for large area sensors and solar cells*. Thin Solid Films. 1999 (337); 1 - 2; 240 - 247

22. J. K. Rath et.al. *Low-temperature deposition of polycrystalline silicon thin films by hot-wire CVD*. Solar Energy Materials and Solar Cells. 1997 (48); 1 - 4; 269 - 277

23. Imaizumi et. al. *Effect of grain size and dislocation density on the performance of thin film polycrystalline silicon solar cells*. Journal of Applied Physics. 1997 (81); 7635

24. Benoit Gaury et. al. *Quantitative Theory of the Grain Boundary Impact on the Open-Circuit Voltage of Polycrystalline Solar Cells*. ACS Applied Energy Materials. 2019 (2); 1; 144 - 151

25. L. Wang et.al. *Low temperature growth of crystalline silicon thin films by ECR plasma CVD for solar cells*. 2nd World Conference and Exhibition on Photovoltaic Solar Energy Conversion, Vienna. 1998

26. G. Andrä et.al. *Multi-crystalline Silicon Thin Films: Laser Crystallization Conditions and Properties*. Solid State Phenomena. 1999 (67 - 68); 187 - 192

27. Ammon W., Sattler A., Kissinger G. *Defects in Monocrystalline Silicon*. Springer Handbook of Electronic and Photonic Materials. 2017

28. Jean de Dieu Mugiraneza et.al. *Structural Characterization of Sputtered Silicon Thin Films after Rapid Thermal Annealing for Active-Matrix Organic Light Emitting Diode*. The Japan Society of Applied Physics. 2010 (49); 12R

29. A. Lambertz et.al. *Sputter deposited and solid phase crystallized silicon films for solar cells*. 2nd World Conference and Exhibition on Photovoltaic Solar Energy Conversion, Vienna. 1998.

30. R.L. Wallace et.al. *Low-cost thin-film silicon for terrestrial solar cells*. Photovoltaics Program Review. Proceedings of the 14th Conference. 1996; 511

31. Louise R. Bailey et.al. *High rate amorphous and crystalline silicon formation by pulsed DC magnetron sputtering deposition for photovoltaics*. Phys. Status Solidi (A). 2015 (212); 1; 42 - 46

32. Koji Yamasaki et.al. *Crystallization of an Amorphous Si Thin Film by Using Pulsed Rapid Thermal Annealing with Ni-Ferritin*. Journal of the Korean Physical Society. 2010 (56); 3

33. R. Gunawan et.al. *Optimal control of rapid thermal annealing in a semiconductor process*. Journal of Process Control. 2004 (14); 423 - 430

34. M. Cardona. *Vibrational Spectra of Hydrogen in Silicon and Germanium*. Physica Status Solidi (b). 1983 (118); 463

35. David Tuschel. *Micro-Raman Spectroscopy of Crystal Lattice Chemistry*. Spectroscopy. 2012 (27); 3

 doi:10.20944/preprints202007.0274.v1

36. Mahieu et.al. *Biaxial alignment in sputter deposited thin films*. Thin Solid Films. 2006 (515); 1229 - 1249

37. Perkin Elmer. The Use of UV/Vis/NIR Spectroscopy in the Development of Photovoltaic Cells. 2009

38. Tauc, J. *Optical properties and electronic structure of amorphous Ge and Si*. Materials Research Bulletin 1968(3); 37- 46